Industrial Crops & Products 226 (2025) 120646

Contents lists available at ScienceDirect

Industrial Crops & Products

journal homepage: www.elsevier.com/locate/indcrop

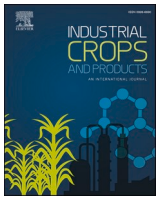

Iron and nitrogen co-doping biochar for simultaneous and efficient adsorption of oxytetracycline and norfloxacin from wastewater

Xiaoxue Cheng [a,b], Ding Jiang [a], Weiyi Zhu [a], Huan Xu [a], Qifan Ling [a], Jingwen Yang [a], Xinyu Wang [a], Kexin Zhang [a], Xiaolong Zheng [a], Sirong He [a], Bin Cao [c], Stuart Wagland [b], Shuang Wang [a,*]

[a] School of Energy and Power Engineering, Jiangsu University, Jiangsu 212013, China
[b] School of Water, Energy and Environment, Cranfield University, Cranfield MK43 0AL, UK
[c] Korea Biochar Research Center and the Division of Environmental Science and Ecological Engineering, Korea University, Seoul 02841, Republic of Korea

ARTICLE INFO

Keywords:
Biochar
Antibiotic removal
Langmuir isotherm
Cooperative Chemisorption
π-π interactions
Orbital hybridization

ABSTRACT

The global proliferation of antimicrobial resistance (AMR) poses a critical challenge to environmental and public health, driven by excessive antibiotic release from medical, agricultural, and aquaculture activities. This study investigates the synthesis and application of Fe/N-doped biochar derived from *Enteromorpha clathrata (EC)* for the removal of oxytetracycline (OTC) and norfloxacin (NOR) from water. The biochar, synthesized via pyrolysis and NaOH activation, was characterized by BET, SEM, and XPS analyses, revealing a porous structure with enriched functional groups. The EC-derived biochar demonstrated high adsorption capacities for OTC (625.325 $mg \cdot g^{-1}$) and NOR (487.379 $mg \cdot g^{-1}$) under neutral pH conditions, with adsorption following Langmuir and pseudo-second-order models, indicative of monolayer chemisorption. The biochar also exhibited excellent reusability, supporting practical applications. The strong interactions between the FeN_4 active sites and the antibiotics were quantified through DFT calculations, showing binding energies of −394.91 kcal/mol for NOR and −398.10 kcal/mol for OTC, highlighting the important role of FeN_4 in facilitating efficient adsorption. Additionally, density of states (DOS) analysis revealed that formation of Fe-N/O chemical bonds was confirmed through the hybridization of Fe 3d orbitals with N/O 2p orbitals. Overall, Fe/N-rich biochar contributes to its potential for practical applications in antibiotic removal from aqueous systems.

1. Introduction

Antibiotics are essential in preventing and treating diseases across medical, agricultural, and aquaculture sectors (Song et al., 2023; Kaur Sodhi and Singh, 2022). Although global initiatives aim to reduce antibiotic use, market projections suggest that its value could reach USD 1.57 trillion by 2024 (Verma et al., 2022). However, antimicrobial resistance (AMR) has emerged as a severe global health threat, underscored by the United Nations Environment Programme (UNEP) *Frontiers 2017* report (UNEP, 2017). This report estimates that nearly 700,000 people die each year from infections caused by antibiotic-resistant pathogens that existing antibiotics can no longer effectively treat (UNEP, 2017). The environment now plays a major role in the spread of antibiotic resistance, with wastewater from households, hospitals, and agricultural runoff containing antimicrobial agents, fostering direct interactions between natural microbial communities and resistant bacteria, thereby accelerating the emergence of resistant strains (UNEP, 2017). Following antibiotic usage, up to 80 % of these drugs remain unmetabolized and are excreted into the environment via urine and feces, along with resistant bacteria (Quaik et al., 2020). This issue is further intensified by the rising antibiotic demand; human antibiotic consumption has increased by 36 % in the past decade, while antibiotic use in livestock is expected to grow by 67 % by 2030 (Quaik et al., 2020). Additionally, as much as 75 % of antibiotics used in aquaculture may leach into surrounding environments, presenting serious ecological risks (Quaik et al., 2020).

Moreover, agricultural irrigation often relies on water drawn from surrounding sources, including reclaimed wastewater (RWW) from households, hospitals, and agricultural runoff, which frequently contains antibiotics (Christou et al., 2017). The use of RWW for crop

* Corresponding author.
E-mail address: alexjuven@ujs.edu.cn (S. Wang).

https://doi.org/10.1016/j.indcrop.2025.120646
Received 3 December 2024; Received in revised form 27 January 2025; Accepted 1 February 2025
Available online 11 February 2025

irrigation (Chen et al., 2016; Kama et al., 2024) has raised concerns about prolonged exposure of agricultural environments to antibiotics, antibiotic-resistant bacteria (ARB), and antibiotic resistance genes (ARG). Evidence suggests that antibiotics and ARGs may spread in agricultural soils due to RWW irrigation and the application of fertilizers or biosolids. Residual antibiotics in soils can undergo adsorption/desorption and transformation processes (both biotic and abiotic), potentially affecting soil microbial communities and health. Antibiotics in soil pore water—the bioavailable fraction—may be absorbed by crops, bioaccumulate in plant tissues, (Wu et al., 2018; Han et al., 2017; Zhou et al., 2024; Li et al., 2024a; Yang et al., 2024) and subsequently enter the food web, (Zhang et al., 2024; Shoaib et al., 2024; Li et al., 2021; Gan et al., 2021) leading to potential public health risks (Zeng et al., 2020; Jiang et al., 2018; Marimuthu et al., 2021). These findings underscore the necessity of treating wastewater to reduce antibiotic contamination, ensuring it meets government standards for agricultural irrigation.

Wastewater treatment plants are unable to completely remove antibiotics and resistant bacteria, creating potential hotspots for resistance. Studies have documented the widespread presence of multidrug-resistant bacteria in seawater and sediments near aquaculture, industrial, and municipal discharge sites (Xue et al., 2022). B. S. Choudri (Al-Riyami et al., 2018) provides a review on antibiotics in wastewater with a focus on Oman. Researchers have also evaluated the occurrence, fate and removal of pharmaceuticals in sewage and sludge samples collected from the largest sewage sewer plant in southern Brazil (Bisognin et al., 2021). Chen et al. (2017) detected 9 antibiotics in pig farm wastewater, including sulfamethoxazine, sulfachlorpyridazine, sulfamethoxazine, trimethoprim, norfloxacin, ofloxacin, lincomycin, Leukomycin and oxytetracycline at concentrations up to 192,000 ng/L. Numerous studies have shown that multiple antibiotics coexist in wastewater (Christou et al., 2017). Among various antibiotics, oxytetracycline (OTC) is extensively used in animal husbandry, aquaculture, and human medicine, contributing significantly to environmental contamination (Feng et al., 2021; Liu et al., 2023). Due to its high stability and resistance, OTC persists in the environment, leading to the spread of antibiotic-resistant genes and posing risks to aquatic ecosystems and human health (Zhang et al., 2022a, 2022b). Similarly, norfloxacin (NOR), a commonly used fluoroquinolone (FQ) antibiotic, demonstrates strong antibacterial activity against both gram-negative and gram-positive bacteria by inhibiting DNA gyrase (Picó and Andreu, 2007; Ahmed and Theydan, 2014). Due to its persistence, NOR can accumulate in the environment, promoting bacterial resistance and posing ecological risks (Hirsch et al., 1999). Key pathways for NOR entry into surface waters include manure application as fertilizer and leakage from septic systems. Studies have detected NOR in surface water and wastewater effluents at concentrations up to 0.036 μg/L and 0.45 μg/L, respectively (Batt et al., 2007). Although these concentrations appear low, the continuous introduction of NOR into aquatic environments can lead to its accumulation, increasing risks to aquatic and terrestrial organisms over time (Ahmed and Theydan, 2014). Consequently, the removal of antibiotics from wastewater is a critical environmental challenge, necessitating the development of efficient and practical methods for their removal.

Adsorption has become one of the most effective strategies for wastewater treatment due to its simplicity, cost-effectiveness, and avoidance of secondary pollution (Wang et al., 2021; Jiang et al., 2024). However, adsorption efficiency is significantly influenced by the chemical structures of both the adsorbent and the adsorbate, presenting challenges in designing high-efficiency adsorbents. The adsorption performance of carbon-based materials for organic contaminants is largely determined by their pore structure and surface functional groups (Biswal and Balasubramanian, 2022; Zhang et al., 2011). Oxytetracycline (OTC), as an amphoteric molecule, contains various functional groups—such as phenol, amino, alcohol, and olefin ketone—that can exhibit diverse charges or electronic coupling behaviors depending on the pH conditions (Ahmed et al., 2016). Similarly, the molecular structure of norfloxacin (NOR) enables it to interact with adsorbent surfaces through hydrogen bonding and coordination interactions (Ahmed and Theydan, 2014). Adsorbents with a well-developed pore structure and abundant aromatic groups, especially those with electron-donating functionalities, can significantly enhance the adsorption of both OTC and NOR. These materials not only offer ample adsorption sites through their porous framework but also facilitate specific interactions with these antibiotics, thereby improving adsorption efficiency (Zhou et al., 2023).

Biochar, a carbon-rich material derived from biomass pyrolysis, (Zhang et al., 2019a; Jing et al., 2019; Qiu et al., 2023) has gained significant attention as an adsorbent (Fan et al., 2024; Li and Cheng, 2023; Tian et al., 2023; Xue et al., 2024; Yang et al., 2023; Zhang et al., 2023). Its high surface area, porosity, and versatile surface chemistry make it effective in removing pollutants, (Fan et al., 2022; Zhang et al., 2019b; Liu et al., 2020) including antibiotics, from water. Typically, biochar is chemically activated using agents such as KOH, NaOH, $ZnCl_2$, and H_3PO_4 to increase its specific surface area (Liu et al., 2016). In particular, KOH activation substantially enhances the surface area and porosity of biochar, thereby improving its adsorption capacity for organic pollutants (Luo et al., 2018). Additionally, nitrogen-modified biochar exhibits enhanced adsorption capabilities due to the incorporation of nitrogen, which introduces additional active sites for electrostatic interactions (Guy Laurent Zanli et al., 2022). Nitrogen doping not only increases biochar's specific surface area and microporous structure but also incorporates nitrogen-containing functional groups that significantly improve its ability to adsorb organic pollutants like norfloxacin. Key nitrogen functionalities introduced during doping—such as pyridinic-N, pyrrolic-N, and graphitic-N—not only enhance biochar's hydrophilicity and polarity but also strengthen antibiotic adsorption through mechanisms like hydrogen bonding and π-π interactions. High-temperature N-doped biochar exhibits a strong micropore-filling capacity, resulting in greater adsorption capacity and stability under environmental conditions. Recent studies (Jiang et al., 2024; Liu et al., 2021) also indicate that biochar modified with metals (Qin et al., 2023) or metal oxides (Xiansheng et al., 2023) significantly improves adsorption performance. For example, Mg/Fe bimetallic oxide-modified biochar demonstrated enhanced adsorption capacities for pollutants, achieving up to 206.2 mg/g for oxytetracycline under optimal conditions. Such modifications not only boost adsorption capacity but also facilitate the separation of biochar from water, making it more practical for wastewater treatment applications (Jiang et al., 2024).

Traditionally, biochar has been produced from various biomass sources, including agricultural residues like rice husk, (Li et al., 2020) corn straw, (Deng et al., 2022) and groundnut shells (Shakya et al., 2022). However, these materials often require additional chemical activation, nitrogen doping, and modification with metals or metal oxides to enhance their surface area and adsorption capacity (Song et al., 2023). In contrast, *Enteromorpha clathrata* (*EC*), a type of marine biomass, offers inherent advantages as a raw material for biochar production. EC naturally contains high levels of nitrogen and iron, providing a basis for developing Fe/N-doped biochar with enhanced adsorption efficiency. Combining the intrinsic properties of EC with chemical activation using NaOH further increases the biochar's porosity and surface reactivity, resulting in an adsorbent with superior performance for removing contaminants such as antibiotics (Wei et al., 2022; Zhiyu et al., 2023) and dyes (Cheng et al., 2024, 2023; Jiang et al., 2023) from water. This unique blend of natural and synthetic modifications makes EC-derived biochar a highly effective and sustainable solution for environmental remediation.

In this study, *Enteromorpha clathrata* (*EC*), naturally rich in nitrogen and iron, was used as a raw material to develop Fe/N-enriched biochar through a two-step process involving pyrolysis and NaOH chemical activation. The characteristics of the resulting biochar were systematically analyzed using BET surface area measurement, scanning electron microscopy (SEM), and X-ray photoelectron spectroscopy (XPS) to

confirm its structural and surface properties. The primary objective of this study is to evaluate the simultaneous adsorption of two antibiotics, oxytetracycline (OTC) and norfloxacin (NOR), from aqueous solutions. Batch experiments were designed to identify the optimal conditions for the simultaneous removal of these antibiotics, focusing on parameters such as pH, initial concentration, and contact time. In addition to evaluating adsorption kinetics and isotherms, this study investigates the underlying adsorption mechanisms, focusing on the role of Fe-N-C active sites and interactions such as hydrogen bonding, π-π interactions, and electrostatic forces. Reusability tests were performed to assess the stability and regeneration potential of the biochar, indicating its suitability for practical applications. The insights gained from this study contribute to the development of advanced biochar-based materials, offering a sustainable solution for environmental remediation and promoting the utilization of marine biomass resources in pollution control.

2. Materials and methods

2.1. Experiments

The detailed descriptions of materials (**Text S1**), preparation methods (**Text S2**), characterization techniques (**Text S3**), and adsorption experiments (**Text S4–5**) are provided in the supporting information. Briefly, the materials used include dried *Enteromorpha clathrata* (*EC*) powder, oxytetracycline (OTC), and norfloxacin (NOR). The biochar was prepared using a two-step pyrolysis and activation method. The *Enteromorpha clathrata* semi-char (*ECSC*) and *Enteromorpha clathrata* activated carbon (*ECAC*) were synthesized. Characterization of the biochar involved techniques such as SEM, BET surface area analysis, and XPS. The adsorption experiments assessed the performance of the biochar under various conditions, including different dosages, pH levels, and initial concentrations, and included kinetic, isotherm, and regeneration studies.

2.2. Calculation methods

Building on the work of Hou et al. (2012), which explored interactions between nitrogen (N) dopants and native point defects in graphene using density functional theory (DFT), our computational study examines the effects of nitrogen doping and iron (Fe) adsorption on the electronic and structural properties of graphene. The computational models included pristine graphene (PG), N-doped structures with pyrrolic (PN5) and pyridinic (PN6) configurations at edge defects, pyrrole-like (DVN) and pyridine-like (MVN) configurations in bulk defects, and Fe-doped graphene (FeN_4). These models (Fig. 1) were designed to elucidate the impact of nitrogen doping and Fe adsorption on graphene's properties. The pristine graphene (PG) model, constructed using a hexagonal unit cell of pure carbon atoms arranged in a honeycomb lattice, served as a reference for evaluating the effects of nitrogen doping and Fe adsorption. The pyrrolic nitrogen-doped graphene (PN5) model incorporates nitrogen atoms into pentagonal ring defects at the graphene edges, forming a pyrrolic structure (Fig. 1**b**), where the nitrogen atom is part of a five-membered ring. The pyridinic nitrogen-doped graphene (PN6) model (Fig. 1**c**) introduces nitrogen atoms into hexagonal ring defects at graphene edges, creating a pyridinic structure, with nitrogen positioned within a six-membered ring. Introducing nitrogen atoms into monovacancy sites within the graphene body creates a pyridine-like structure (MVN) (Fig. 1**d**), characterized by a nitrogen atom bonded to two carbon atoms with the remaining carbons forming a hexagonal ring (Hou et al., 2012). Nitrogen incorporation into divacancy sites results in a pyrrole-like structure (DVN) (Fig. 1**e**), where a nitrogen atom is part of a five-membered ring, accompanied by an eight-membered carbon ring in the center (Hou et al., 2012). In the FeN_4 model (Fig. 1**f**), an Fe atom is coordinated at the center of a four-nitrogen doped divacancy site, forming a tetrahedral geometry. All DFT calculations were performed using the Gaussian 16 (Frisch et al., 2016) software with the M06–2X functional and 6–31 G(d) basis set, incorporating dispersion corrections and asymmetry

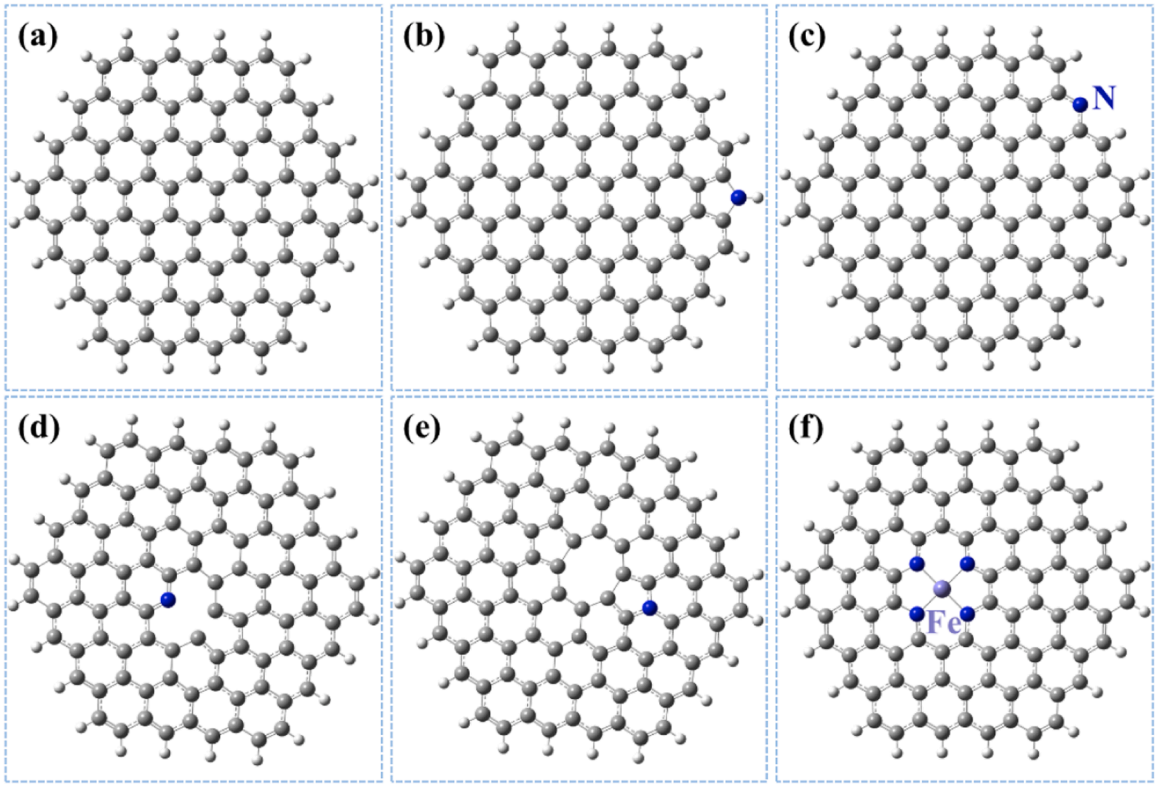

Fig. 1. The six models were investigated: (a) pristine graphene (PG), (b-c) pyrrole-like (PN5) and pyridine-like (PN6) N-doped in the edge defects of graphene, (d-e) pyridine-like (MVN) and pyrrole-like (DVN) N-doped in the bulk defects of graphene, (f) FeN_4.

adjustments for structural optimizations and frequency calculations. Visualizations of weak interactions were generated using VMD, (Humphrey et al., 1996) and quantum chemical wavefunction analyses were conducted with the Multiwfn (Lu, 2024) program. For further details on calculation parameters, refer to our previous work (Cheng et al., 2024, 2023; Jiang et al., 2023).

3. Results and discussions

3.1. Condition optimization

3.1.1. Adsorbent dosage

Fig. 2 shows the effect of adsorbent dosage on the adsorption capacity and removal rate of OTC and NOR in both single (S) and binary (B) systems. In Fig. 2**a**, the removal percentages of OTC and NOR are displayed at varying dosages. As the dosage increases from 0.02 g to 0.10 g, the removal percentages for both antibiotics increase substantially. This trend, observed in both single and binary systems, indicates that higher dosages provide more active sites, enhancing removal efficiency. Fig. 2**b** illustrates the adsorption capacity (mg/g) of the adsorbent for OTC and NOR. At lower dosages, the adsorption capacity is initially high but decreases with increasing dosage, likely due to particle aggregation at higher dosages, which reduces the available surface area. The results suggest an optimal dosage of 0.04 g, where the removal percentage is maximized without significantly lowering adsorption capacity. This balance is essential for designing efficient adsorption systems in water treatment applications.

3.1.2. Effect of initial solution pH

Fig. 2**c** illustrates the effect of pH on the adsorption of OTC and NOR in single and binary systems. The removal percentages of both antibiotics vary with pH, peaking around pH 5–7 for both systems. At extreme pH values (1 and 9), removal efficiency decreases. This pH dependency can be attributed to the ionization states of the antibiotics and the surface charge of the adsorbent. At low pH, the positively charged adsorbent surface may experience electrostatic repulsion with the positively charged antibiotic molecules, reducing adsorption efficiency. In contrast, at high pH, the surface becomes negatively charged, potentially enhancing adsorption of positively charged antibiotic species through electrostatic attraction. However, extremely high pH can also lead to deprotonation of functional groups on the adsorbent, reducing the number of active sites available. The optimal pH range for maximum removal of OTC and NOR is between 5 and 7, which is essential for practical applications in effective water treatment.

The pKa values of NOR are 6.34 and 8.75 (Table S1), indicating two proton binding sites (carboxyl and piperazine groups). Based on pH, NOR exists in different forms: positively charged (NOR^{+}) at pH < 6.34, zwitterionic ($NOR^{\pm}$) at 6.34 < pH < 8.75, and negatively charged (NOR^{-}) at pH > 8.75. As shown in Fig. 2**c**, the removal rate of NOR by ECAC rises from 87.9 % to 97.6 % with increasing pH, then gradually decreases to 74.9 %. The adsorption mechanisms include hydrogen bonding, π-π interactions, Lewis acid-base effects, and electrostatic interactions. The C═O groups of ECAC can form hydrogen bonds with the -OH or -NH_2 groups of NOR, and ECAC's -OH groups can interact with the C═O groups of NOR. Additionally, pyrrolic nitrogen in ECAC can act as a Lewis base, binding with Lewis acid sites (-OH) on NOR, thus enhancing adsorption. The strong electronegativity of F in NOR enables

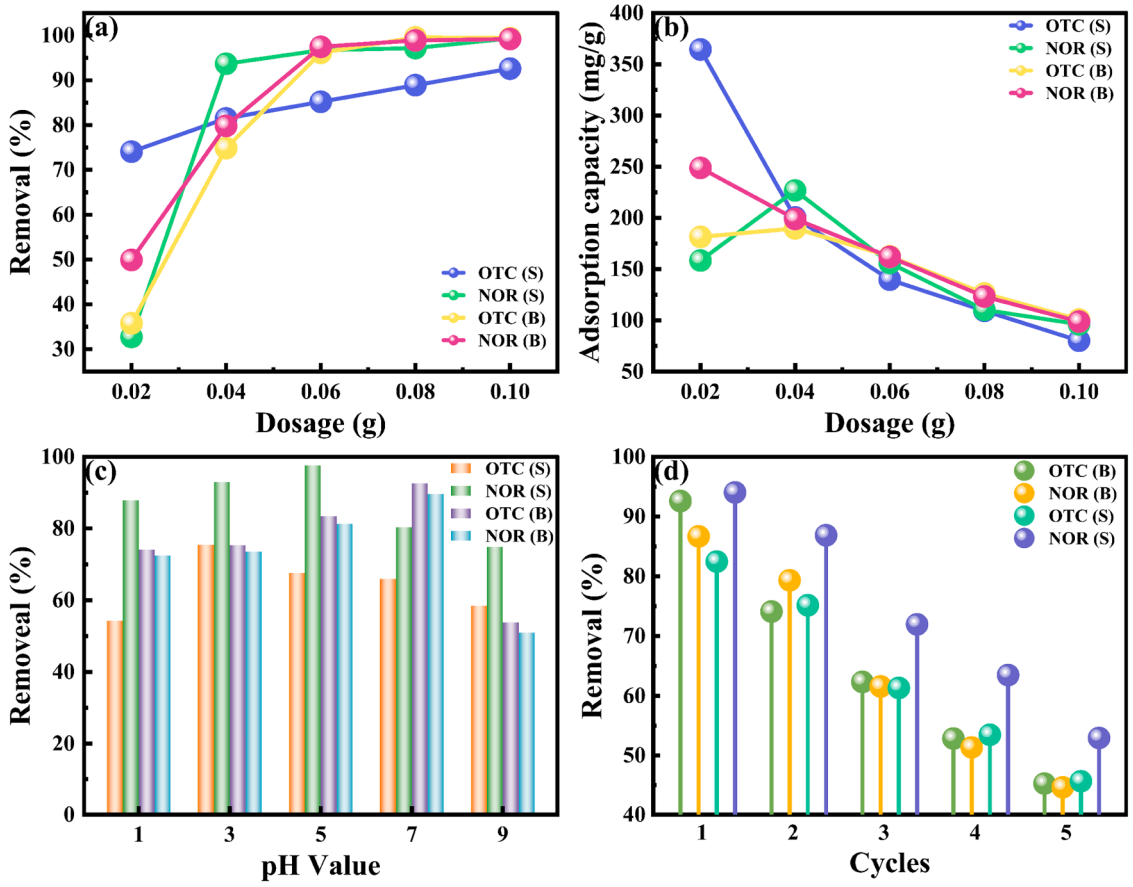

Fig. 2. The effect of (a, b) adsorbent dosages and (c) pH on the adsorption capacity in single and binary systems; (d) adsorption-desorption cycles of ECAC. The experiments were conducted at natural pH and ambient temperature, with an initial antibiotic concentration of 20 mg/L for each compound and a contact time of 24 hours, unless otherwise specified for specific experimental purposes.

π-π interactions with ECAC. At pH < 5, the reduction in NOR^{+} and corresponding decrease in electrostatic repulsion with the positively charged ECAC surface increase adsorption. At pH > 7, the increased presence of NOR^{-} and its electrostatic repulsion with the negatively charged ECAC surface reduce adsorption. Furthermore, NOR deprotonation in alkaline conditions weakens hydrogen bonding, further reducing adsorption capacity.

The pKa values of OTC are 3.27, 7.32, and 9.11 (Table S1), indicating various ionization states: OTC^{+} at pH < 3.27, $OTC^{\pm}$ at 3.27 < pH < 7.32, and OTC^{-}/OTC^{2-} at pH > 7.32. The adsorption capacity of OTC increases with pH, peaks, and then declines (Fig. 2**c**). The adsorption mechanisms of ECAC include hydrogen bonding, π-π interactions, Lewis acid-base effects, and electrostatic interactions. OTC's conjugated enone structure enhances the electron-withdrawing capacity of the ketone group, influencing its π-acceptor properties. The phenol, hydroxyl (-OH), amine, and enone (CH_2=C═O) groups of OTC can form hydrogen bonds with ECAC's surface hydroxyl groups. At pH < 3.27, the reduced presence of OTC^{+} diminishes electrostatic repulsion with ECAC's positive charges, enhancing adsorption. At pH > 3, increasing levels of OTC^{-} and OTC^{2-} heighten electrostatic repulsion with ECAC's negative charges, decreasing adsorption. The ionization of OTC's -OH groups with increasing pH weakens hydrogen bonding, further limiting adsorption.

The adsorption efficiencies of NOR and OTC in single and binary systems are strongly pH-dependent, highlighting electrostatic interactions as a primary mechanism. At pH < 7, ECAC's adsorption capacity for OTC increases while that for NOR decreases, with both peaking at pH 7. This suggests that, below pH 7, competition between NOR and OTC occurs, with OTC demonstrating a competitive advantage, implying that additional mechanisms beyond electrostatic interactions influence adsorption under these conditions. Optimizing adsorbent dosage and initial solution pH is critical for maximizing ECAC's adsorption efficiency for OTC and NOR. Higher dosages increase removal percentages but may reduce adsorption capacity due to particle aggregation. The optimal pH range for effective adsorption is between 5 and 7, consistent with the ionization states of the antibiotics and the adsorbent's surface charge properties. These findings provide practical guidelines for applying ECAC in water treatment systems to efficiently remove antibiotic contaminants.

3.1.3. Practical Application and Reusability

Reusability is a critical factor in the practical application of adsorbents. The adsorption-desorption cycles (Fig. 2**d**) of the biochar show that it retains a high adsorption capacity over multiple cycles, demonstrating strong potential for use in water treatment systems. This reusability is essential for assessing the economic viability and sustainability of the adsorbent in large-scale applications. Additionally, the optimal adsorption conditions identified in this study, such as neutral pH and suitable adsorbent dosages, align well with practical water treatment requirements. The biochar's effectiveness across various pH levels enhances its applicability in diverse water treatment environments. The use of *EC*, an abundant and renewable biomass, adds to the environmental sustainability of the biochar production process. Utilizing this biomass not only provides a cost-effective raw material but also helps manage its overgrowth in coastal regions, addressing an environmental issue. Compared to commercially available activated carbons, the biochar synthesized in this study offers a potentially lower-cost alternative due to the inexpensive feedstock and relatively simple synthesis process. This economic benefit, combined with its high adsorption capacity and reusability, makes the biochar a promising candidate for practical water treatment applications.

3.2. Batch adsorption experiment

3.2.1. Adsorption kinetics

The adsorption kinetics of ECAC for OTC and NOR in single and binary systems were analyzed using three models: the pseudo-first-order (PFO), the pseudo-second-order (PSO), and the intraparticle diffusion models. The fitting curves are presented in Fig. 3, and the model parameters are provided in Tables S3-S6. In the case of the single system, both the PFO and PSO models provided an adequate fit for the adsorption process. The PSO model demonstrated a slightly superior fit, suggesting that the adsorption process may entail chemisorption through valence forces, characterized by electron sharing or exchange between the adsorbent and the adsorbate. In the binary system, analogous trends were observed, with both the PFO and PSO models demonstrating excellent fits. The PSO model exhibited higher R (Kaur Sodhi and Singh, 2022) values, thereby reinforcing the role of chemisorption in the adsorption process. Accordingly, the adsorption kinetics of both OTC and NOR onto ECAC were optimally represented by the PSO model, indicating that chemisorption is the primary mechanism. The model demonstrated robust adsorption capabilities for both OTC and NOR, with NOR exhibiting slightly superior performance. Furthermore, the intraparticle diffusion model posits that the adsorption process comprises multiple steps, with an initial rapid adsorption phase followed by slower intraparticle diffusion. These findings highlight the potential of ECAC as an effective adsorbent for the removal of antibiotics from aqueous solutions, offering valuable insights into the adsorption mechanisms and the influence of antibiotic properties on adsorption performance.

3.2.2. Adsorption isotherms

The adsorption isotherms of ECAC for OTC and NOR in both single and binary systems were analyzed using the Langmuir and Freundlich models. The fitting curves are shown in Fig. 4, and model parameters are listed in Tables S7–S10. The Langmuir isotherm model, which assumes monolayer adsorption on a surface with a finite number of identical sites, provided the following parameters: For the single system, the Langmuir parameters for OTC and NOR are shown in Tables S7 and S8, respectively. The maximum adsorption capacity (qm) for OTC reached 215.066 $mg{\cdot}g^{-1}$ at 30°C, while for NOR, it was 256.027 $mg{\cdot}g^{-1}$ at the same temperature. The R^2 values ranged from 0.795 to 0.844 for OTC and 0.851–0.889 for NOR, indicating a reasonable fit to the Langmuir model. In the binary system, the qm values for OTC and NOR increased significantly, with OTC reaching up to 625.325 $mg{\cdot}g^{-1}$ and NOR 487.379 $mg{\cdot}g^{-1}$ at 30°C. The R^2 values were also higher in the binary system, particularly for NOR, where R^2 ranged from 0.972 to 0.978, indicating a stronger fit to the Langmuir model.

The Freundlich isotherm model, which describes adsorption onto a heterogeneous surface with non-uniform adsorption energy distribution, provided additional insights. For the single system, the Freundlich parameters for OTC and NOR are shown in Tables S7 and S8. The *kF* values for OTC ranged from 60.772 to 150.830 $L{\cdot}mg^{-1}$, and for NOR, from 140.357 to 199.497 $L{\cdot}mg^{-1}$. R^2 values for the Freundlich model were slightly lower than for the Langmuir model, indicating a less optimal fit. In the binary system, the Freundlich parameters for OTC and NOR are listed in Tables S9 and S10, with *kF* values reaching a maximum of 161.697 $L{\cdot}mg^{-1}$ for OTC and 230.150 $L{\cdot}mg^{-1}$ for NOR at 30°C. The R^2 values were generally higher in the binary system, suggesting an improved fit compared to the single system.

Overall, the adsorption isotherms of OTC and NOR onto ECAC were well described by both Langmuir and Freundlich models. However, the Langmuir model generally provided a better fit, particularly in the binary system, as evidenced by higher R^2 values. The maximum adsorption capacities (*qm*) from the Langmuir model were notably higher in the binary system for both OTC and NOR, indicating enhanced adsorption performance in the presence of both antibiotics. The Freundlich model parameters also suggested favorable adsorption, with k_F values indicating strong adsorption capacity, and *1/n* values less than 1, supporting favorable adsorption conditions and surface heterogeneity. These findings underscore the potential of ECAC as an effective adsorbent for removing antibiotics from aqueous solutions, providing valuable insights into the adsorption mechanisms and the influence of antibiotic

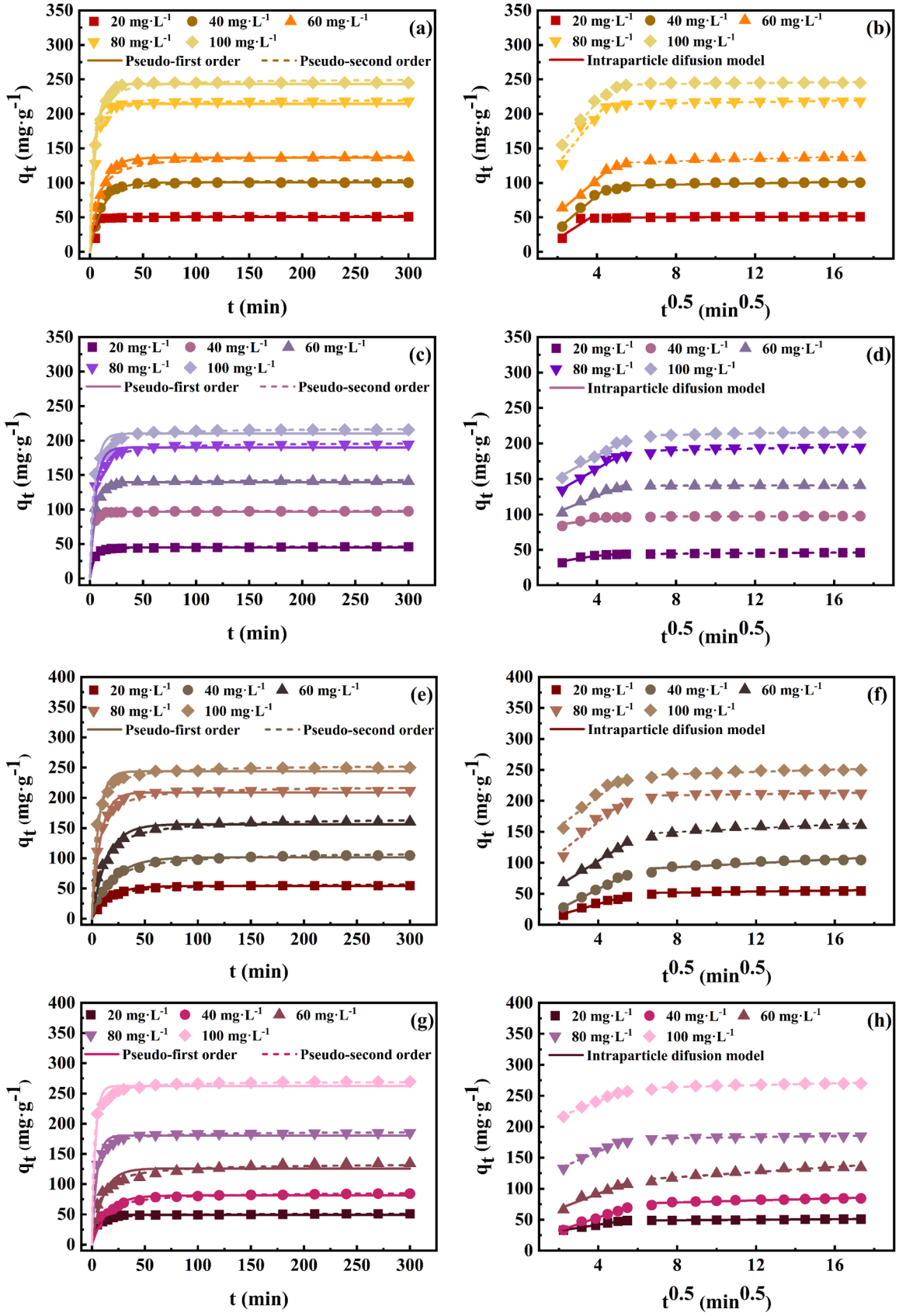

Fig. 3. Adsorption kinetics model. (a-b) is the adsorption kinetics for OTC in a single system. (c-d) is the adsorption kinetics for NOR in a single system. (e-f) is the adsorption kinetics for OTC in a binary system. (g-h) is the adsorption kinetics for NOR in a binary system.

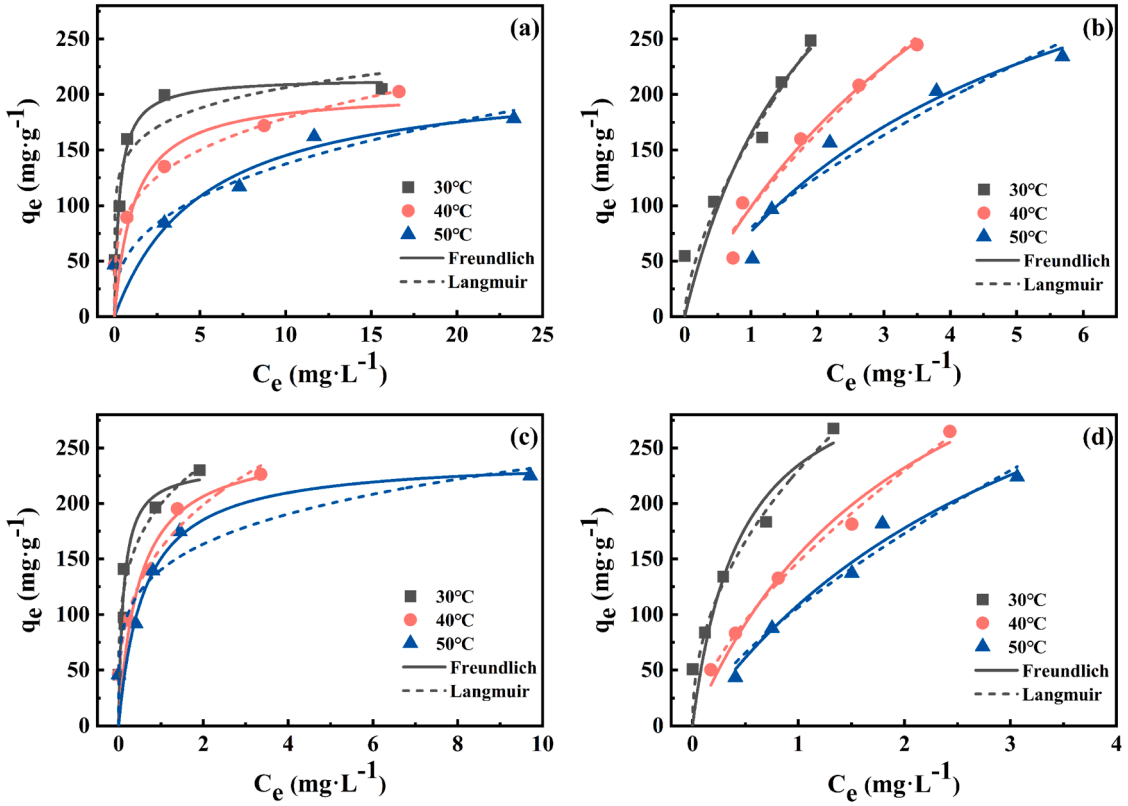

Fig. 4. Adsorption isotherms model. (a-b) is the adsorption isotherms for OTC and NOR in a single system. (c-d) is the adsorption isotherms for OTC and NOR in a binary system.

properties on adsorption performance.

To evaluate the effectiveness of the adsorbent synthesized in this study for antibiotic removal, it was compared with adsorbents synthesized from over 15 different biomass feedstocks in previous studies (Tables S11-S12). The comparison reveals that the biochar (ECAC) derived from Enteromorpha in this study exhibits excellent adsorption performance, particularly in aqueous systems with coexisting antibiotics, where its co-adsorption capacity is significantly enhanced. For NOR, the maximum adsorption capacity of ECAC reached 256.027 mg·g^{-1} in a single-component system and an impressive 487.379 mg·g^{-1} in a binary system. Similarly, for OTC, ECAC demonstrated a maximum adsorption capacity of 215.066 mg·g^{-1} in the single system, which increased substantially to 625.325 mg·g^{-1} in the binary system. These findings highlight the potential of ECAC as an efficient adsorbent for antibiotic removal in water treatment applications. Additionally, the table presents pore structure parameters of each adsorbent, indicating that these parameters play a critical role in adsorption capacity. This key observation provides a foundation for further investigation in this study, which will be discussed in detail below.

3.3. Characterization of the activated carbons

3.3.1. BET Surface Area and Pore Size Distribution Analysis

The surface area and pore structure analysis of ECSC and ECAC reveal substantial differences in their physical properties, which can be attributed to variations in their preparation and activation processes. Table 1 presents the BET surface area, micropore surface area, total pore volume, micropore volume, average pore diameter, and mesopore diameter for both samples. Fig. 5 illustrates the nitrogen (N_2) adsorption-desorption isotherms and pore size distribution of ECSC and ECAC, providing visual confirmation of the quantitative data in Table 1.

As shown in Table 1, the BET surface area (S_{BET}) of ECAC reaches

Table 1
The surface properties of *ECSC* and *ECAC*.

Sample	S_{BET} ($m^2 \cdot g^{-1}$)	t-Plot S_{micro} ($m^2 \cdot g^{-1}$)	V_{total} ($m^3 \cdot g^{-1}$)	t-Plot V_{micro} ($m^3 \cdot g^{-1}$)	D_{ave} (nm)	BJH D_{meso} (nm)
ECSC	1.85	0.24	0.007	0.000	16.54	16.02
ECAC	898.62	717.02	0.642	0.320	2.86	5.61

898.62 $m^2 \cdot g^{-1}$, which is significantly higher than that of *ECSC*, measured at only 1.85 $m^2 \cdot g^{-1}$. This large discrepancy indicates that *ECAC* underwent a more extensive activation process, resulting in a porous structure with significantly more accessible surface area. The high surface area of *ECAC* is advantageous for adsorption and catalysis, as it offers a greater number of active sites. The micropore surface area (t-Plot S_{micro}) of *ECAC*, calculated at 717.02 $m^2 \cdot g^{-1}$, is also considerably larger than that of *ECSC* (0.24 $m^2 \cdot g^{-1}$), suggesting that *ECAC* has a well-developed microporous structure. This is further supported by the N_2 adsorption-desorption isotherm in Fig. 5(a), where *ECAC* exhibits a type I isotherm characteristic of microporous materials, with a sharp increase in nitrogen uptake at low relative pressure. In contrast, *ECSC* shows almost no adsorption across the pressure range, indicating a lack of developed porosity. The total pore volume (V_{total}) of ECAC is 0.642 $m^3 \cdot g^{-1}$, which is significantly higher than that of *ECSC* (0.007 $m^3 \cdot g^{-1}$). Additionally, the micropore volume (t-Plot V_{micro}) for *ECAC* is 0.320 $m^3 \cdot g^{-1}$, accounting for nearly 50 % of the total pore volume. These findings confirm that *ECAC* has a highly microporous structure, providing ample pore volume for potential adsorption applications. The pore size distribution curve in Fig. 5**(b)** reveals that *ECAC*'s pores are primarily within the micropore range, with a distribution peaking around 5 nm, further emphasizing its suitability for adsorbing small molecules. In terms of average pore diameter (D_{ave}) and mesopore diameter (BJH D_{meso}), *ECAC* exhibits values of 2.86 nm and 5.61 nm,

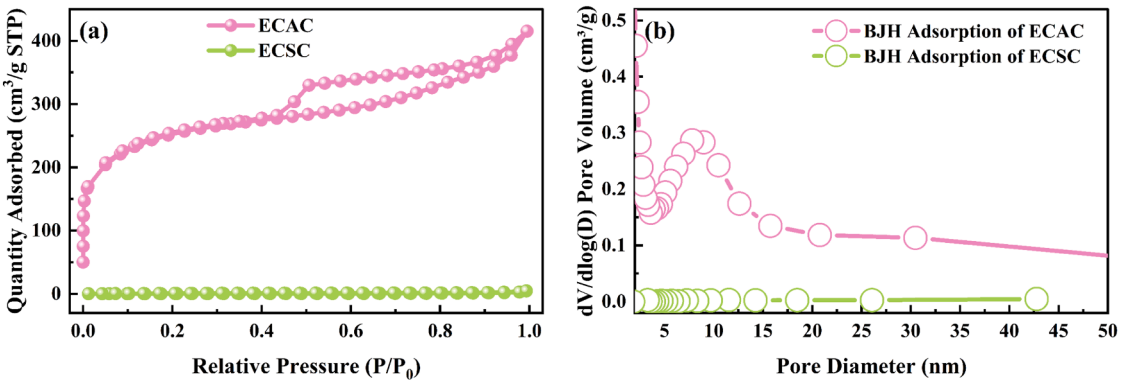

Fig. 5. (a) N_2 adsorption-desorption isotherm and (b) pore size distribution of *ECSC* and *ECAC*.

respectively, indicating the presence of both micropores and small mesopores. This distribution is beneficial for adsorption processes that require molecular sieving effects. Conversely, *ECSC* has a larger average pore diameter (16.54 nm) and mesopore diameter (16.02 nm), suggesting a structure dominated by a few larger pores rather than a well-developed porous network, as confirmed by the low adsorption observed in its isotherm and pore volume data.

In summary, the BET and pore size distribution analyses, supported by Table 1 and Fig. 5, illustrate that *ECAC* possesses a highly porous structure with an extensive microporous network, making it highly suitable for applications requiring high surface area and efficient adsorption. *ECSC*, with its limited porosity and low surface area, would be less effective for such applications. These findings highlight the importance of activation in developing porous carbons for specific adsorption and catalytic functions.

3.3.2. *SEM Analysis of Adsorbent Morphology*

The SEM images presented in Fig. 6 provide insights into the surface morphology of *ECAC* before and after the adsorption of the antibiotics OTC and NOR, both individually and in combination. These morphological observations highlight the structural changes that occur as a result of the adsorption process.

Fig. 6**a** shows the SEM image of pristine *ECAC*, where the surface exhibits a highly porous and rough texture. The presence of numerous pores and irregularities on the surface suggests that *ECAC* has a substantial surface area, which is advantageous for adsorption applications. This rough and porous morphology is indicative of a material with a high adsorption capacity, as it provides multiple active sites for capturing contaminants. The high surface area observed in the SEM images aligns well with the BET analysis, which confirms the well-developed porous structure of *ECAC*. Fig. 6**b** illustrates the morphology of *ECAC* after adsorption of OTC (denoted as OTC@*ECAC*). The surface of the adsorbent appears more aggregated and compact compared to the pristine state. This aggregation is likely due to the deposition of OTC molecules onto the *ECAC* surface and within its pores. The filled pores and smoother appearance of the surface indicate that OTC has successfully adsorbed onto the *ECAC*, effectively occupying the available adsorption sites. This morphological change suggests that the adsorbent structure adapts to accommodate OTC molecules, leading to a less porous, more compact morphology. Fig. 6**c** shows the SEM image of *ECAC* after adsorption of NOR (NOR@*ECAC*). Similar to the case with OTC, the surface of the adsorbent after NOR adsorption appears denser and more consolidated. There is a noticeable reduction in visible pores, implying that NOR molecules have also effectively occupied the

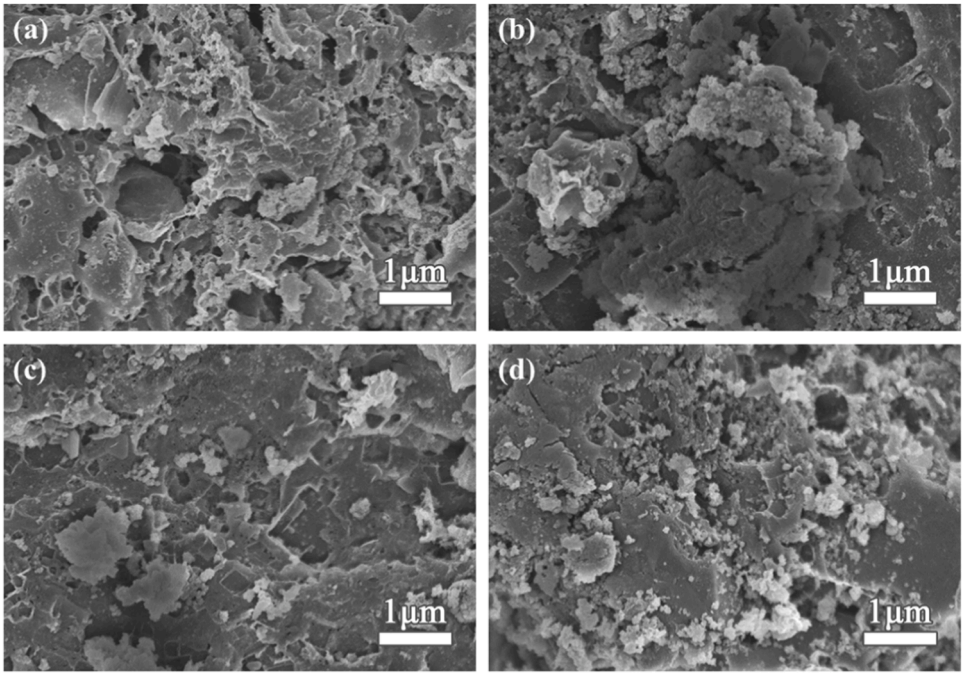

Fig. 6. SEM of (a)*ECAC*, (b)OTC@*ECAC*, (c)NOR@*ECAC*, (d) OTC/NOR@*ECAC*.

adsorption sites on *ECAC*. This denser structure is indicative of a successful adsorption process, where NOR molecules integrate into the *ECAC* matrix, reducing its initial porosity and resulting in a more packed morphology. In Fig. 6**d**, the SEM image of *ECAC* after the simultaneous adsorption of both OTC and NOR (OTC/NOR@*ECAC*) displays significant aggregation and a highly compact surface. The combined presence of OTC and NOR results in a more pronounced filling of the pores and surface coverage than observed in the single-component adsorption cases. This compact structure suggests that *ECAC* can effectively adsorb multiple antibiotics simultaneously, demonstrating a high affinity for both OTC and NOR. The dense morphology highlights the adsorbent's capacity to capture and hold a substantial amount of contaminants within its porous framework.

In summary, the SEM analysis demonstrates that *ECAC* undergoes notable morphological changes upon the adsorption of OTC and NOR, both individually and together. The adsorption process transforms the initially porous and rough surface into a more aggregated and compact structure. These changes in surface morphology confirm the successful interaction between *ECAC* and the antibiotics, underscoring the potential of *ECAC* as an effective adsorbent for removing antibiotic contaminants from aqueous solutions. The substantial surface coverage and pore filling observed in the SEM images suggest that *ECAC* is a viable candidate for water treatment applications targeting the simultaneous removal of multiple antibiotic pollutants.

3.3.3. *XPS Analysis of Elemental Composition and Functional Groups*

X-ray photoelectron spectroscopy (XPS) was utilized to analyze the surface chemistry of the *ECAC* adsorbent before and after adsorption of the antibiotics OTC and NOR, both individually and in combination. This analysis sheds light on the elemental composition and functional groups of *ECAC*, revealing how surface functionalities interact with these antibiotics. The primary elements identified in the XPS spectra (Fig. 7) include carbon (C 1 s), nitrogen (N 1 s), oxygen (O 1 s), iron (Fe), and fluorine (F). The elemental compositions in Table 2 show that pristine *ECAC* contains 49.70 % carbon, 7.08 % nitrogen, 33.72 % oxygen, and 9.51 % iron. The nitrogen and iron present in *ECAC* confirm successful doping, enhancing the adsorption properties of the biochar by introducing additional active sites that facilitate interactions with contaminants. Previous studies (Wang et al., 2008, 2013) suggest that the enrichment of N and Fe in biochar results from activation and carbonization processes, which favor the formation of Fe-N-C active sites.

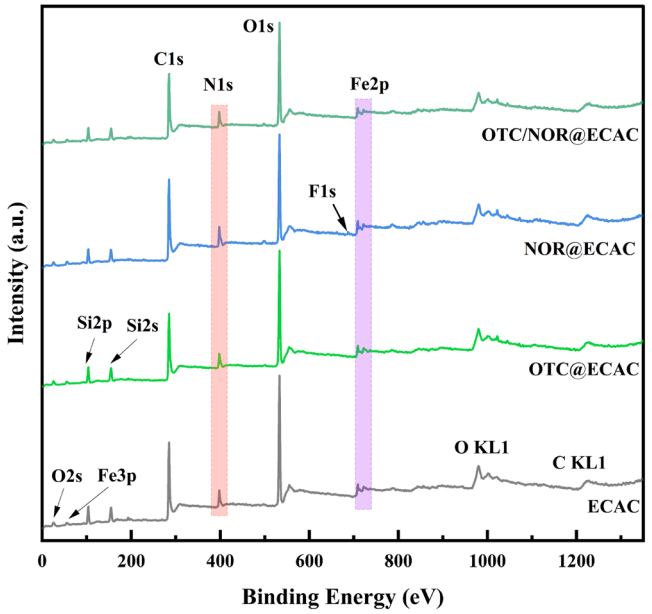

Fig. 7. XPS spectra of *ECAC* before and after adsorption.

Table 2
Various Element content (%) in the samples based XPS survey spectrum.

Samples	C 1 s	N 1 s	O 1 s	F 1 s	Fe
ECAC	49.70	7.08	33.72	-	9.51
OTC@*ECAC*	49.32	7.02	33.21	-	10.45
NOR@*ECAC*	52.66	8.42	27.74	1.67	9.52
OTC/NOR@*ECAC*	52.58	7.18	31.19	0.13	8.91

These sites play a pivotal role in improving adsorption through enhanced interaction with pollutants (Cheng et al., 2024, 2023; Jiang et al., 2023). Upon adsorption of OTC, the carbon content decreases slightly to 49.32 %, while iron content increases to 10.45 %, indicating that OTC primarily interacts with iron sites on the *ECAC* surface. This interaction is likely facilitated by coordination with Fe-N-C sites, enhancing adsorption capacity. NOR adsorption, on the other hand, increases the carbon content to 52.66 % and nitrogen to 8.42 %, with the appearance of 1.67 % fluorine, confirming successful NOR adsorption. The increased nitrogen content suggests strong interactions with nitrogen functionalities, while fluorine acts as a unique marker for NOR. For dual adsorption of OTC and NOR, carbon and nitrogen contents remain high (52.58 % and 7.18 %, respectively), with a trace amount of fluorine (0.13 %), indicating ECAC's capacity for simultaneous antibiotic adsorption.

Detailed functional group analysis (Fig. 8 and Table 3) highlights changes in binding energies and atomic percentages for C 1 s, N 1 s, and O 1 s before and after adsorption. The C 1 s spectrum of *ECAC* reveals multiple carbon-containing functional groups, with a prominent peak for C═C bonds (21.26 %), indicative of aromatic and graphene-like structures that facilitate π-π interactions with aromatic contaminants (Cheng et al., 2024, 2023; Jiang et al., 2023). The high proportion of hydroxyl groups in the O 1 s spectrum is crucial for hydrogen bonding and electrostatic interactions, enhancing the adsorbent's affinity for antibiotics. Other oxygen functionalities, such as carbonyl and carboxyl groups, though less abundant, further contribute to adsorption capacity by providing additional active sites. In the N 1 s spectrum, pyridinic-N (60.44 %) is the predominant nitrogen species, with contributions from pyrrolic-N, graphitic-N, and nitrogen-oxygen functionalities. Pyridinic-N and graphitic-N provide basicity and electron-donating properties, which favor interactions with acidic antibiotic molecules. The Fe-N bonds, observed at lower binding energies, suggest iron incorporation into the *ECAC* matrix, likely enhancing the material's magnetic properties and facilitating easy separation after adsorption. Upon adsorption of OTC and NOR, significant shifts occur in binding energies and intensities for functional groups in the C 1 s, N 1 s, and O 1 s spectra. The increased C═O content after antibiotic adsorption points to coordination interactions between antibiotics and carbonyl groups on *ECAC*. In the N 1 s spectrum, changes in nitrogen content and binding energy after NOR adsorption suggest strong interactions with nitrogen functionalities, potentially involving hydrogen bonding or electrostatic attraction. Additionally, the O 1 s spectrum shows increased C═O after OTC adsorption, indicating possible coordination with carbonyl groups, while the C-OH increase after NOR adsorption suggests hydrogen bonding. These XPS findings highlight the complex interactions between *ECAC* and the antibiotics OTC and NOR, involving both physical adsorption and chemical interactions through hydrogen bonding and coordination with surface functionalities. The presence of Fe-N-C sites and the observed fluorine in NOR further confirm that modified activated carbons, especially those with iron, possess enhanced adsorption capacity for antibiotics. The combined effects of increased surface area, diverse functional groups, and metal-nitrogen bonds underscore the potential of *ECAC* in water treatment applications for effective antibiotic removal.

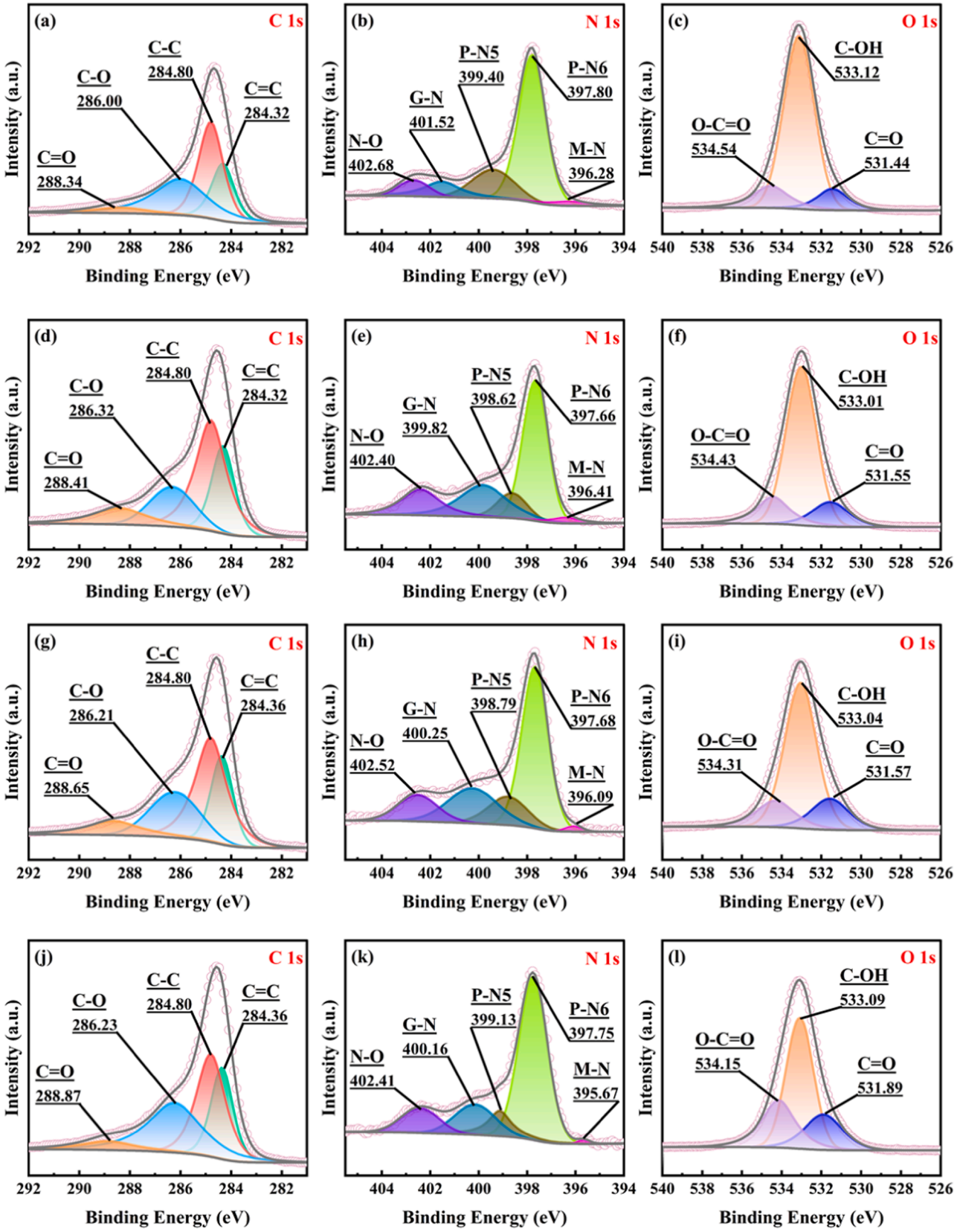

Fig. 8. XPS fine spectra of C 1 s, N 1 s and O 1 s of (a-c) *ECAC*, (d-f) OTC@*ECAC*, (g-i) NOR@*ECAC*, (j-l) OTC/NOR@*ECAC*.

Table 3
Various functional groups and proportions based XPS fine spectrum.

	Name	*ECAC*		OTC@*ECAC*		NOR@*ECAC*		OTC/NOR@*ECAC*	
		B.E. (eV)	Atomic (%)	B.E. (eV)	Atomic (%)	B.E. (eV)	Atomic (%)	B.E. (eV)	Atomic (%)
C 1 s	C═C	284.32	21.26	284.32	23.50	284.36	22.07	284.36	23.51
	C-C	284.80	39.06	284.80	44.10	284.80	41.48	284.80	35.87
	C-O	286.00	34.02	286.32	20.42	286.21	25.38	286.23	34.06
	C═O	288.34	5.66	288.41	11.98	288.65	11.07	288.87	6.56
N 1 s	M-N	396.28	3.77	396.41	3.15	396.09	1.33	395.67	0.97
	P-N6	397.80	60.44	397.66	48.35	397.68	51.27	397.75	60.05
	P-N5	399.40	18.37	398.62	10.44	398.79	13.58	399.13	10.85
	G-N	401.52	10.07	399.82	22.5	400.25	21.13	400.16	16.04
	N-O	402.68	7.35	402.40	15.55	402.52	12.70	402.41	12.09
O 1 s	C═O	531.44	10.32	531.55	13.91	531.57	17.41	531.89	20.55
	C-OH	533.12	76.58	533.01	70.73	533.04	66.84	533.09	53.02
	O-C═O	534.54	13.10	534.43	15.36	534.31	15.75	534.15	26.42

3.4. Adsorption mechanisms

3.4.1. Medicine Molecular Properties

Density Functional Theory (DFT) calculations were employed to analyze the molecular properties of the antibiotics OTC and NOR, providing insights into their structural and electronic characteristics that influence their adsorption behavior on ECAC. The DFT-calculated molecular properties, including dimensions, molar volume, dipole moment, polarizability, and molecular orbital energies, are summarized in Table 4.

The molecular dimensions of OTC and NOR reveal differences in length, width, and height, which impact their ability to fit into various pore sizes on the adsorbent surface. OTC has a length of 13.75 Å, a width of 10.18 Å, and a height of 8.47 Å, whereas NOR is slightly longer at 15.53 Å, but with a narrower width (9.83 Å) and a shorter height (5.89 Å). The compact shape of NOR suggests that it may more easily access smaller pores within the ECAC structure compared to the bulkier OTC molecule. This size difference influences their adsorption efficiency, as NOR may fit more effectively into micropores or smaller mesopores, while OTC might require larger pore spaces for effective adsorption. The molar volumes of OTC (297.77 $cm^3 \cdot mol^{-1}$) and NOR (223.94 $cm^3 \cdot mol^{-1}$) further highlight their structural disparity, with OTC having a larger molar volume, consistent with its bulkier structure. This larger volume may hinder OTC's diffusion into narrow pores, leading to differences in adsorption dynamics when compared to NOR. The dipole moments of the two molecules also vary significantly, with NOR exhibiting a higher dipole moment of 7.52 Debye compared to 5.16 Debye for OTC. The higher dipole moment of NOR indicates a stronger polarity, which could enhance its interaction with polar functional groups (such as hydroxyl and carbonyl) on the ECAC surface, favoring adsorption through dipole-dipole interactions or hydrogen bonding. The polarizability values, calculated as 264.92 a.u. for OTC and 202.22 a.u. for NOR, provide further insights into their interaction potential with the adsorbent. The higher polarizability of OTC suggests that it can undergo greater induced polarization upon interaction with ECAC, potentially enhancing van der Waals interactions. However, the lower polarizability of NOR might be compensated by its higher dipole moment, which strengthens its electrostatic interactions with polar surface sites on ECAC. In terms of electronic properties, the HOMO (highest occupied molecular orbital) and LUMO (lowest unoccupied molecular orbital) energies reflect the electron-donating and accepting abilities of OTC and NOR. The HOMO energy of OTC is −0.28 Hartree, slightly lower than NOR's HOMO energy of −0.26 Hartree, indicating that OTC may be a better electron donor. However, both antibiotics exhibit similar LUMO energies, with OTC at −0.05 Hartree and NOR at −0.01 Hartree. The energy gap (ΔE) between the HOMO and LUMO is a critical factor in determining the chemical reactivity of a molecule. OTC and NOR have small energy gaps (0.23 Hartree for OTC and 0.25 Hartree for NOR), suggesting they are both relatively reactive and likely to engage in electron transfer or charge transfer interactions with the active sites on ECAC.

These DFT-calculated molecular properties align well with the single system adsorption experimental results, where NOR exhibits a higher maximum adsorption capacity (q_{max}= 256.027 $mg \cdot g^{-1}$) compared to

Table 4
DFT Calculated Medicine Molecular Properties of OTC and NOR.

Property		OTC	NOR
3D model		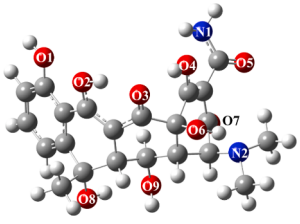	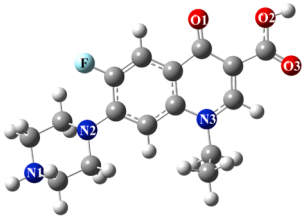
Length of the sides (Å)	Length	13.75	15.53
	width	10.18	9.83
	height	8.47	5.89
Molar volume (cm^3/mol)		297.77	223.94
Dipole Moment (Debye)		5.16	7.52
Polarizability (α) (a.u.)		264.92	202.22
Energy (Hartree)		−1638.16	−1109.52
HOMO (Hartree)		−0.28	−0.26
LUMO (Hartree)		−0.05	−0.01
Gap (Hartree) = LUMO-HOMO		0.23	0.25

OTC (q_{max} = 215.066 mg·g^{-1}). The higher q_{max} for NOR can be attributed to its smaller dimensions, stronger polarity, and higher dipole moment, which enhance its interactions with the ECAC surface, especially with polar functional groups. In contrast, OTC's slightly bulkier structure and higher polarizability may favor interactions with hydrophobic or π-π active sites but can limit its accessibility to smaller pores, leading to a somewhat lower adsorption capacity.

In summary, the DFT-calculated molecular properties of OTC and NOR indicate that NOR's smaller dimensions, higher dipole moment, and stronger polarity might favor its interaction with polar functional groups on ECAC, potentially making it more efficient in adsorbing onto polar sites. Conversely, OTC, with its larger polarizability and slightly better electron-donating ability, could interact strongly with hydrophobic or π-π active sites on the adsorbent. These insights suggest that the adsorption behavior of OTC and NOR on ECAC involves a complex interplay of size compatibility, polarity, and electronic properties, which collectively contribute to the observed higher adsorption capacity of NOR over OTC. This finding underscores the efficacy of ECAC in selectively adsorbing antibiotics, highlighting its potential for effective water treatment applications.

3.4.2. *Electron wavefunction analysis and Adsorption energy*

The electrostatic potential surfaces (ESP) and weak interaction visualizations provide a comprehensive understanding of the interactions between various nitrogen- and iron-doped adsorbents and the antibiotics OTC and NOR. By combining ESP mapping with adsorption energy calculations, we can elucidate how specific dopants influence the binding strength and interaction modes with these antibiotics, as shown in Fig. 9 and Fig. 10.

The ESP maps reveal significant charge distribution differences among the doped adsorbents. Pristine graphene (PG) shows a relatively neutral potential, indicating limited affinity for polar molecules, which suggests it may exhibit weak adsorption for OTC and NOR. In contrast, nitrogen-doped models, such as PN5 (pyrrolic nitrogen) and PN6 (pyridinic nitrogen), display distinct charge characteristics. PN6, with a highly negative potential region around the nitrogen site, provides a strong electron-rich area, enhancing electrostatic attraction to the positively polarized regions of NOR, especially its nitrogen atoms. Conversely, PN5 shows a positive potential around the nitrogen, creating an electron-deficient area suitable for interacting with electron-rich sites on OTC. Since both PN5 and PN6 are positioned at the edge of the graphene matrix, they face minimal steric hindrance, allowing antibiotics to interact freely with these reactive sites, thereby facilitating adsorption. The mono- and di-vacancy nitrogen-doped models, MVN and DVN, exhibit nitrogen atoms embedded within the bulk of the structure, leading to significant steric hindrance. This spatial restriction limits the accessibility of antibiotics to these reactive sites, resulting in reduced interaction strength, as reflected in the adsorption energies. Although MVN and DVN introduce electron-rich regions that can potentially attract antibiotics, the spatial constraints weaken these interactions, making MVN and DVN less effective compared to edge-located nitrogen species like PN5 and PN6. The FeN_4 model, featuring an Fe center embedded in a nitrogen-deficient defect site, also resides within the bulk region, similar to MVN and DVN. However, the presence of iron enables strong metal-ligand covalent bonding with highly electronegative atoms (N and O) in the antibiotic molecules, particularly OTC. This metal-covalent bonding significantly diminishes the impact of steric hindrance around the FeN_4 site, allowing Fe to interact effectively with the antibiotics. The high adsorption energies observed for FeN_4—approximately −398.10 kcal·mol^{-1} for OTC and −394.91 kcal·mol^{-1} for NOR—indicate that the metal center plays a crucial role in enhancing binding stability and adsorption strength.

The weak interaction visualizations using Independent Gradient Model Hirshfeld (IGMH) analysis (Fig. 10) further confirm the nature of these interactions. For PG, the green regions around OTC and NOR indicate primarily van der Waals interactions, leading to moderate adsorption energies (-370.19 kcal·mol^{-1} for OTC and −370.60 kcal·mol^{-1} for NOR). However, the FeN_4 model exhibits strong blue regions in the visualizations, reflecting metal-ligand covalent interactions, especially between Fe and the electronegative atoms of OTC and NOR. These interactions significantly enhance binding affinity and adsorption capacity, positioning FeN_4 as an ideal dopant for maximizing adsorption performance. For PN5 and PN6, the IGMH visualizations reveal slightly different interaction profiles for each antibiotic. PN5 shows moderate interaction strength with OTC, where the positive potential around pyrrolic nitrogen interacts with the electron-rich sites of OTC, as reflected in an adsorption energy of −355.19 kcal·mol^{-1}. PN6, on the other hand, shows stronger electrostatic attraction with NOR, due to the alignment of its electron-rich pyridinic nitrogen site with NOR's positively polarized regions, resulting in an adsorption energy of −353.03 kcal/mol. Both PN5 and PN6 benefit from their edge positioning, which reduces steric hindrance and allows antibiotics to interact freely with the reactive sites.

In summary, the combined ESP and IGMH analyses demonstrate that

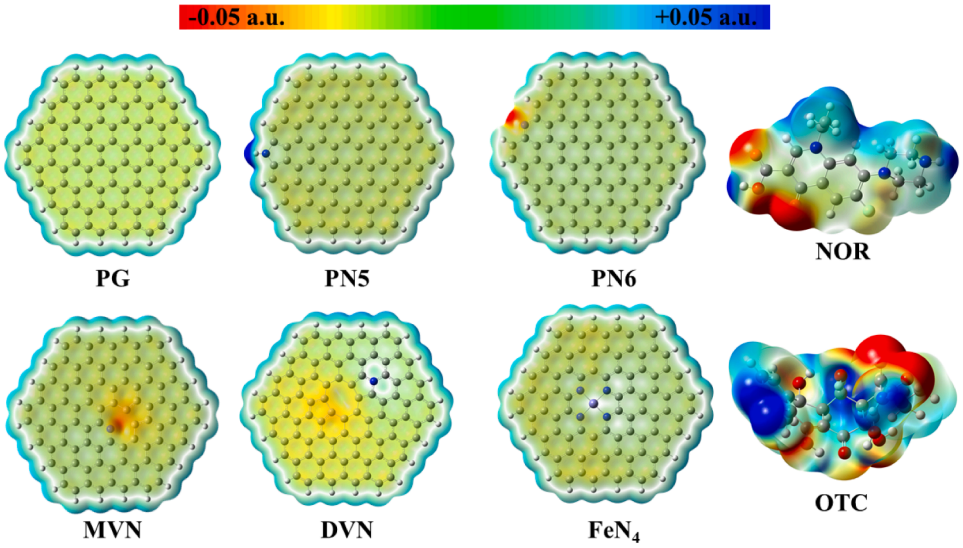

Fig. 9. Molecular surface electrostatic potential of adsorbents and antibiotics. White represents H atoms, light blue represents F atoms, gray represents C atoms, blue represents N atoms, and red represents O atoms.

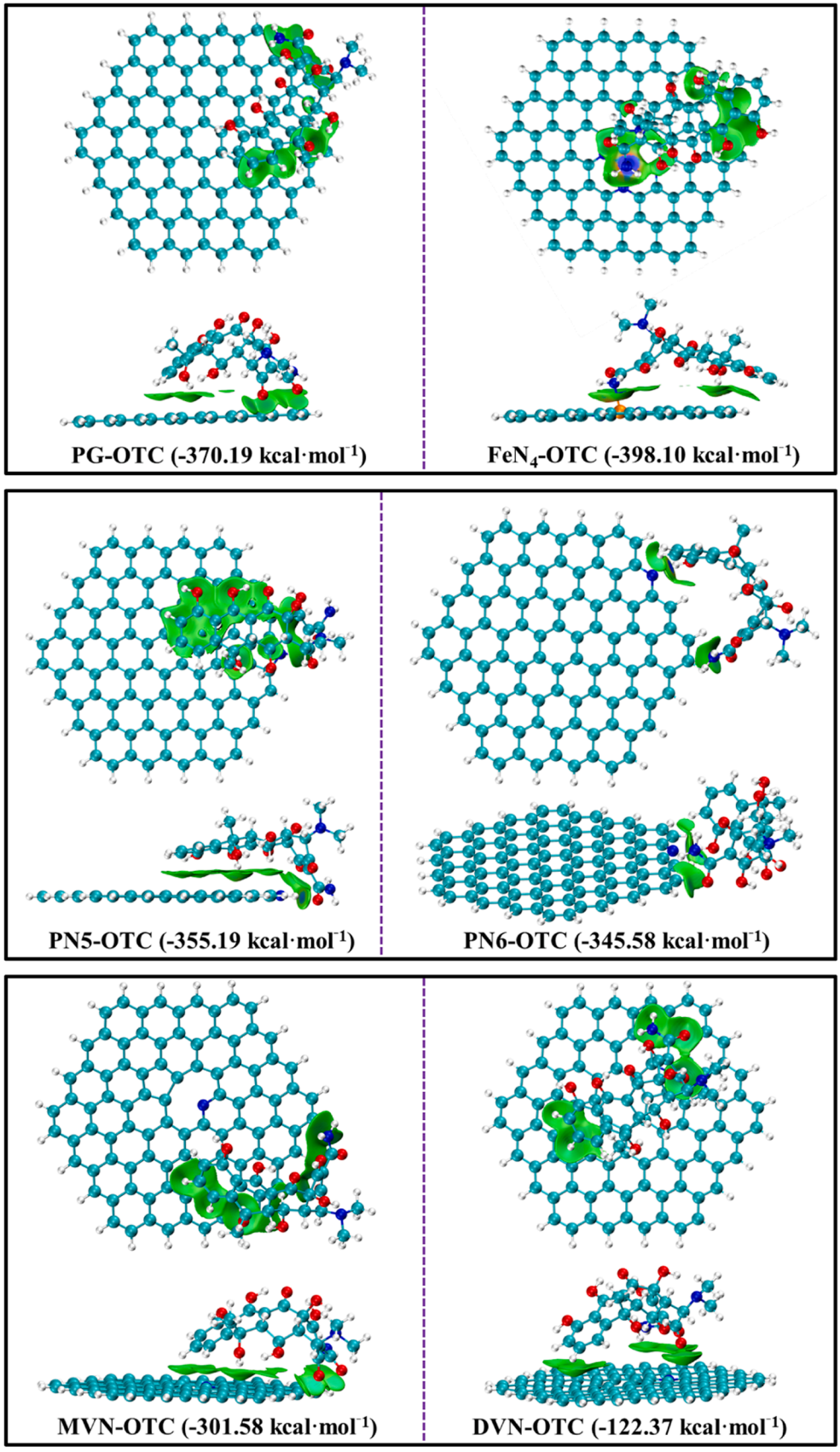

Fig. 10. IGMH visualizations and adsorption energy (ΔE) between antibiotics and adsorbents.

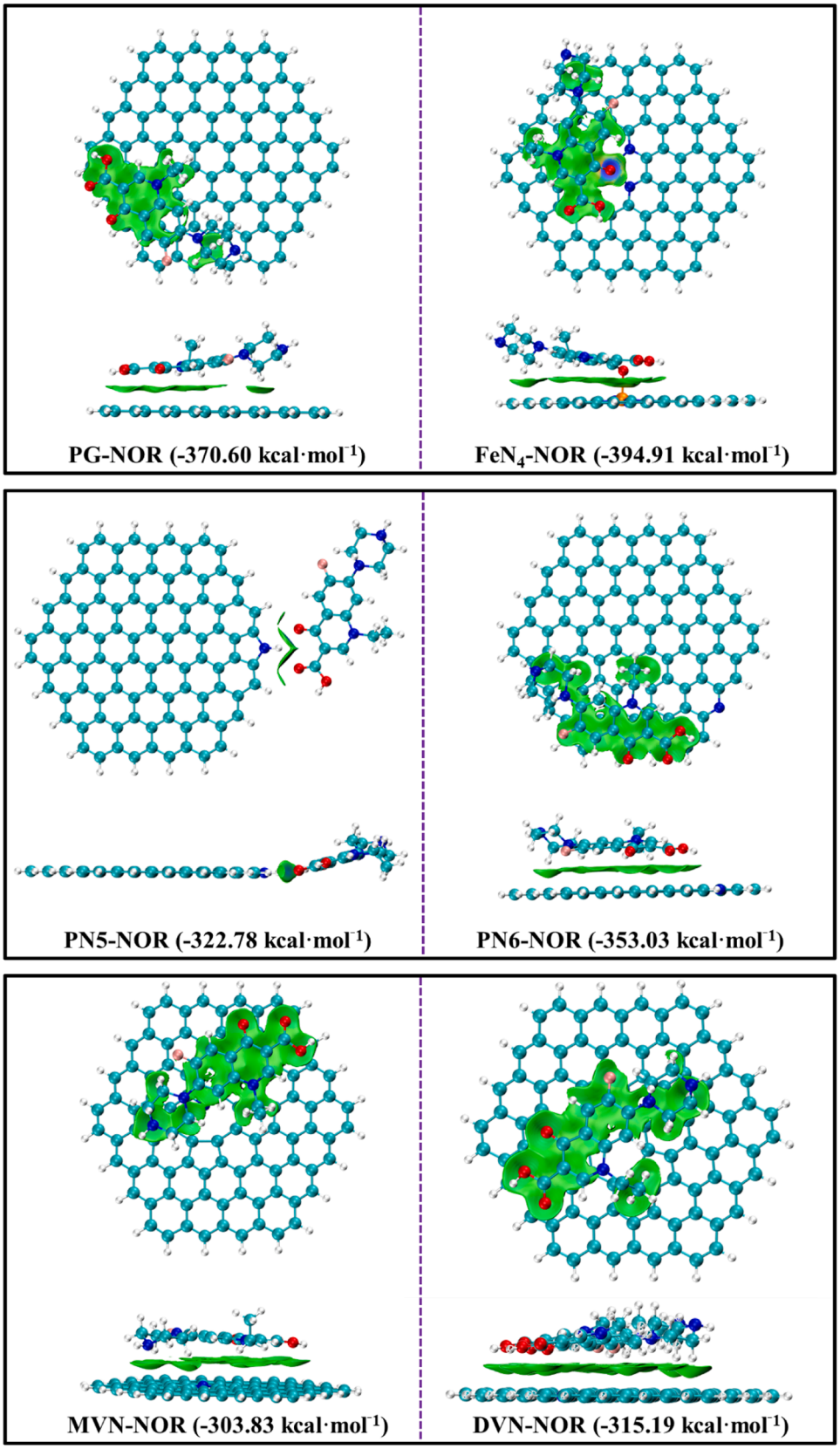

Fig. 10. (*continued*).

nitrogen and iron dopants significantly enhance the adsorption capabilities of biochar surfaces. Edge-positioned nitrogen species, such as PN5 and PN6, offer high accessibility and favorable charge distribution for antibiotic adsorption, while FeN_4, despite its bulk location, overcomes steric hindrance through strong metal-ligand interactions. MVN and DVN, by contrast, exhibit limited adsorption efficiency due to steric

constraints around bulk nitrogen sites. These results underscore the critical role of selective doping strategies in optimizing biochar surfaces for water treatment applications, with Fe and pyridinic nitrogen identified as highly effective dopants for enhancing interaction strength and adsorption stability.

3.4.3. *DOS Analysis for FeN_4 Model Adsorbing NOR and OTC*

The adsorption mechanism of antibiotic molecules on the surface of adsorbents is one of the central topics of this study. To explore this, we calculated the density of states (DOS) for the most stable adsorption configuration, FeN_4. Specifically, we analyzed the following: (i) the changes in the DOS of the antibiotic molecules before and after the adsorption reaction (Fig. 11**a-b**); (ii) the DOS of the Fe atoms, N atoms from OTC, and O atoms from NOR, which directly interact with the FeN_4 surface before and after adsorption (Fig. 11**c-d**); and (iii) the contributions of the atomic orbitals (Fe 3d, N 2p, O 2p) involved in these interactions (Fig. 11**e-f**).

As shown in Fig. 11**a-b**, after the adsorption reaction, the DOS of OTC and NOR molecules exhibit significant changes, primarily observed as a shift of the peak positions towards lower energy regions by approximately 2 eV for OTC and 1 eV for NOR. This suggests that, during the adsorption process, the energy of the antibiotic molecules is lowered, and their molecular structures become more stable. Moreover, OTC appears to be more stable than NOR. Fig. 11**c-d** shows the DOS of the Fe atoms, N atoms of OTC, and O atoms of NOR, which directly interact with the FeN_4 surface before and after adsorption. A distinct peak in the DOS of Fe atoms appears at −3 eV, indicating strong localization of the Fe atoms' valence electrons. By comparing Fig. 11c-d, it is evident that the DOS near the Fermi level (−4 eV to −2 eV) undergoes minimal change, with only a slight shift towards lower energies. However, in the energy range between −6 eV and −4 eV, the peaks in the DOS of the antibiotic molecules show a significant change, with the peak density decreasing. This can be attributed to the formation of Fe-N/O bonds between the surface Fe atoms and the N or O atoms in the antibiotics.

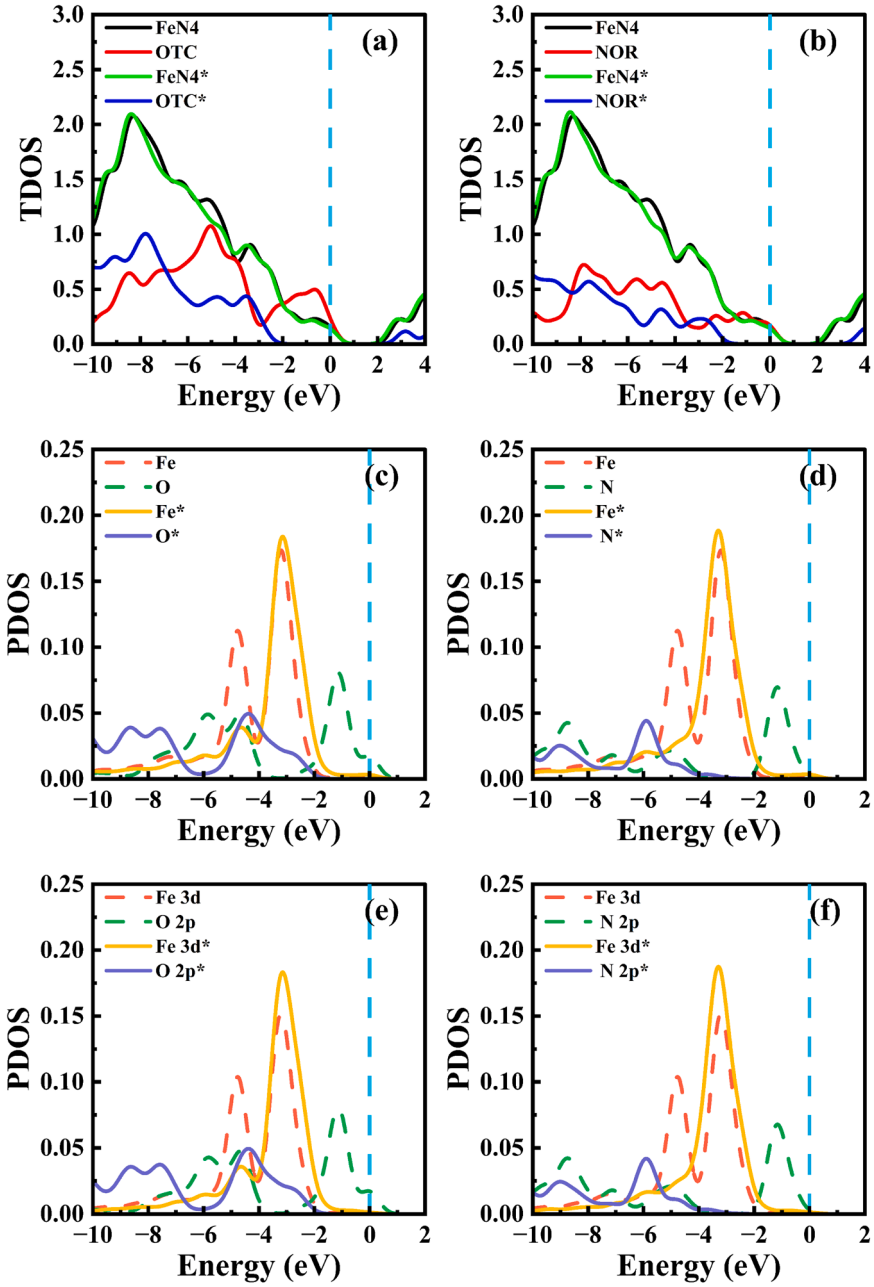

Fig. 11. Density of states (DOS) of FeN_4 model, FeN_4-OTC and FeN_4-NOR. The species after adsorption are marked with an asterisk (*). 0 eV is the Fermi level.

Specifically, the Fe atom in the FeN_4 configuration primarily participates in a four-coordinate structure with four N atoms; however, upon adsorption of the antibiotic molecules, the original coordination network is disrupted.

To further investigate the role of the N or O atoms in the antibiotics and the Fe atoms on the FeN_4 surface during the adsorption reaction, it is necessary to analyze the partial DOS (PDOS) of the adsorbed atoms. As observed in Fig. 11**e**, after the adsorption of OTC molecules, there is significant overlap between the 2*p* orbitals of the O atoms and the 3*d* orbitals of the Fe atoms on the surface. This indicates that the adsorption reaction induces strong hybridization (Wang et al., 2024; Wu et al., 2025) between the 2*p* orbital of O and the 3*d* orbital of Fe, leading to the formation of a Fe-O chemical bond, which demonstrates a chemical interaction between the O atom and the surface Fe atom. Additionally, in the OTC molecule, two main resonance peaks are observed between the 2*p* orbital of the O atom and the 3d orbital of Fe on the FeN_4 surface, with peak positions at −4.5 eV and −2.5 eV. These resonance peaks indicate the formation of Fe-O bonds between the O atoms in the OTC molecule and the Fe atoms on the FeN_4 surface (Fig. 12), which is consistent with the previous analysis. Finally, from Fig. 11**f**, it can be observed that when NOR molecules are adsorbed, a Fe-N chemical bond is also formed. However, the overlap between the 2p orbitals of the N atom and the 3d orbitals of the Fe atoms on the surface is less pronounced, indicating a lower degree of hybridization. This is consistent with the binding energy and IGMH results. In summary, the adsorption mechanism between the antibiotic molecules and the FeN_4 surface is attributed to strong hybridization between the 2p orbitals of the N/O atoms and the 3d orbitals of the Fe atoms, leading to the formation of Fe-N/O chemical bonds (Li et al., 2024b).

Fig. 12 shows the fragment electron density difference in Multiwfn. The yellow and green isosurfaces (+0.004 and −0.004 a.u., respectively) represent the region in which electron density is increased and decreased after NOR or OTC coordinated to FeN4, respectively. In all models, the Fe-N/O bond length is less than or equal to the sum of the atomic radii of the two atoms (Cordero et al., 2008) (with a Fe atom radius of 1.25 Å, an O atom radius of 0.73 Å, and a N atom radius of 0.75 Å). This leads to the conclusion that the FeN_4 collector exhibit strong adsorption and accompanied by the formation of new chemical bonds. On the other hand, investigating electron transfer (as depicted in Fig. 12), yellow indicates charge accumulation, green indicates charge depletion, and the yellow is located just above the Fe-N/O bond, again indicating the formation of a new chemical bond.

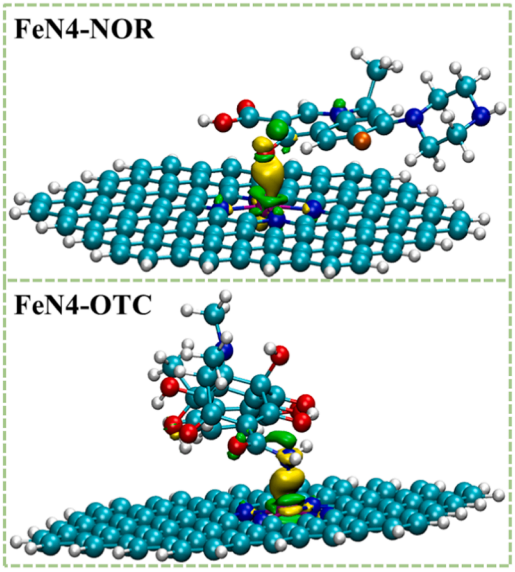

Fig. 12. The electron density difference of FeN_4 adsorption models: NOR and OTC. Investigation of the electron transfer (yellow for charge accumulation and green for charge depletion).

4. Conclusions

This study presents the synthesis and evaluation of a Fe/N-rich biochar derived from EC for the efficient removal of antibiotics from water. The biochar demonstrated high adsorption capacities for OTC and NOR in both single and binary systems, with maximum adsorption capacities reaching 487.379 $mg{\cdot}g^{-1}$ for NOR and 625.325 $mg{\cdot}g^{-1}$ for OTC in binary systems. Characterization analyses revealed that the high surface area, abundant functional groups, and FeN_4 active sites contributed significantly to the biochar's superior adsorption performance. The biochar exhibited good reusability across multiple adsorption-desorption cycles. Adsorption kinetics followed a pseudo-second-order model, suggesting chemisorption as the primary mechanism, while the Langmuir isotherm model provided the best fit for the equilibrium data. The strong interactions between the FeN_4 active sites and the antibiotics were quantified through DFT calculations, showing binding energies of −394.91 kcal/mol for NOR and −398.10 kcal/mol for OTC, highlighting the important role of FeN_4 in facilitating efficient adsorption. Additionally, density of states (DOS) analysis revealed that the FeN_4 sites played a crucial role in the adsorption process. The adsorption of OTC and NOR molecules led to significant changes in the DOS, with a shift in the peak positions towards lower energy regions, indicating that the antibiotic molecules became more stable upon adsorption. The formation of Fe-N/O chemical bonds was confirmed through the hybridization of Fe 3d orbitals with N/O 2p orbitals, particularly in OTC (Fe-O) and NOR (Fe-N). Overall, the Fe/N-rich biochar, particularly through the interaction with FeN_4 sites, demonstrated exceptional adsorption performance, contributing to its potential for practical applications in the removal of antibiotics from aqueous systems.

CRediT authorship contribution statement

Zhu Weiyi: Data curation. **Wang Shuang:** Supervision, Resources, Project administration, Funding acquisition. **Ling Qifan:** Investigation. **Xu Huan:** Data curation. **Wang Xinyu:** Software. **Yang Jingwen:** Investigation. **Zheng Xiaolong:** Validation. **Zhang Kexin:** Software. **Cao Bin:** Writing – review & editing. **He Sirong:** Writing – review & editing. **Jiang Ding:** Supervision, Software, Conceptualization. **Wagland Stuart:** Writing – review & editing. **Cheng Xiaoxue:** Writing – original draft, Validation, Software, Methodology.

Declaration of Competing Interest

The authors declare that they have no known competing financial interests or personal relationships that could have appeared to influence the work reported in this paper.

Acknowledgements

This work was supported by the Jiangsu Province Outstanding Youth Fund (BK20230012) and the High-performance Computing Platform of Jiangsu University.

Appendix A. Supporting information

Supplementary data associated with this article can be found in the online version at doi:10.1016/j.indcrop.2025.120646.

Data availability

Data will be made available on request.

References

Ahmed, M.B., Zhou, J.L., Ngo, H.H., Guo, W., Chen, M., 2016. Progress in the preparation and application of modified biochar for improved contaminant removal from water and wastewater. Bioresour. Technol. 214, 836–851.

Ahmed, M.J., Theydan, S.K., 2014. Fluoroquinolones antibiotics adsorption onto microporous activated carbon from lignocellulosic biomass by microwave pyrolysis. J. Taiwan Inst. Chem. Eng. 45 (1), 219–226.

Al-Riyami, I.M., Ahmed, M., Al-Busaidi, A., Choudri, B.S., 2018. Antibiotics in wastewaters: a review with focus on Oman. Appl. Water Sci. 8 (7), 199.

Batt, A.L., Kim, S., Aga, D.S., 2007. Comparison of the occurrence of antibiotics in four full-scale wastewater treatment plants with varying designs and operations. Chemosphere 68 (3), 428–435.

Bisognin, R.P., Wolff, D.B., Carissimi, E., Prestes, O.D., Zanella, R., 2021. Occurrence and fate of pharmaceuticals in effluent and sludge from a wastewater treatment plant in Brazil. Environ. Technol. 42 (15), 2292–2303.

Biswal, B.K., Balasubramanian, R., 2022. Adsorptive removal of sulfonamides, tetracyclines and quinolones from wastewater and water using carbon-based materials: Recent developments and future directions. J. Clean. Prod. 349, 131421.

Chen, A., Liang, H., Chen, T., Yang, W., Ding, C., 2016. Influence of long-term irrigation with treated papermaking wastewater on soil ecosystem of a full-scale managed reed wetland. J. Soils Sediment. 16 (4), 1352–1359.

Chen, J., Liu, Y.-S., Zhang, J.-N., Yang, Y.-Q., Hu, L.-X., Yang, Y.-Y., Zhao, J.-L., Chen, F.-R., Ying, G.-G., 2017. Removal of antibiotics from piggery wastewater by biological aerated filter system: Treatment efficiency and biodegradation kinetics. Bioresour. Technol. 238, 70–77.

Cheng, X., Jiang, D., Chen, H., Barati, B., Yuan, C., Li, H., Wang, S., 2023. Multi-stage adsorption of methyl orange on the nitrogen-rich biomass-derived carbon adsorbent: DFT and MD evaluation. Chemosphere 338, 139218.

Cheng, X., Li, H., Jiang, D., Lu, W., Ling, Q., Zhong, S., Chen, H., Barati, B., Hu, X., Gong, X., Wang, S., 2024. Insights into simultaneous efficient removal of cationic and anionic dyes by nitrogen-rich seaweed carbon adsorbent. Process Saf. Environ. Prot. 184, 38–49.

Christou, A., Agüera, A., Bayona, J.M., Cytryn, E., Fotopoulos, V., Lambropoulou, D., Manaia, C.M., Michael, C., Revitt, M., Schröder, P., Fatta-Kassinos, D., 2017. The potential implications of reclaimed wastewater reuse for irrigation on the agricultural environment: The knowns and unknowns of the fate of antibiotics and antibiotic resistant bacteria and resistance genes – A review. Water Res. 123, 448–467.

Cordero, B., Gómez, V., Platero-Prats, A.E., Revés, M., Echeverría, J., Cremades, E., Barragán, F., Alvarez, S., 2008. Covalent radii revisited. Dalton Trans. (21), 2832–2838.

Deng, Y., Wang, M., Yang, Y., Li, X., Chen, W., Ao, T., 2022. Enhanced adsorption performance of sulfamethoxazole and tetracycline in aqueous solutions by MgFe2O4-magnetic biochar. Water Sci. Technol. 86 (3), 568–583.

Fan, X., Peng, L., Wang, X., Han, S., Yang, L., Wang, H., Hao, C., 2022. Efficient capture of lead ion and methylene blue by functionalized biomass carbon-based adsorbent for wastewater treatment. Ind. Crops Prod. 183, 114966.

Fan, Z., Zhou, X., Lu, Q., Gao, Z.F., Deng, S., Peng, Z., Han, W., Chen, X., 2024. Synthesis of sewage sludge biochar in molten salt environment for advanced wastewater treatment: Performance enhancement, carbon footprint and environmental impact reduction. Water Res. 250, 121072.

Feng, L., Yuan, G., Xiao, L., Wei, J., Bi, D., 2021. Biochar Modified by Nano-manganese Dioxide as Adsorbent and Oxidant for Oxytetracycline. Bull. Environ. Contam. Toxicol. 107 (2), 269–275.

Frisch, M.J.; Trucks, G.W.; Schlegel, H.B.; Scuseria, G.E.; Robb, M.A.; Cheeseman, J.R.; Scalmani, G.; Barone, V.; Petersson, G.A.; Nakatsuji, H.; Li, X.; Caricato, M.; Marenich, A.V.; Bloino, J.; Janesko, B.G.; Gomperts, R.; Mennucci, B.; Hratchian, H. P.; Ortiz, J.V.; Izmaylov, A.F.; Sonnenberg, J.L.; Williams; Ding, F.; Lipparini, F.; Egidi, F.; Goings, J.; Peng, B.; Petrone, A.; Henderson, T.; Ranasinghe, D.; Zakrzewski, V.G.; Gao, J.; Rega, N.; Zheng, G.; Liang, W.; Hada, M.; Ehara, M.; Toyota, K.; Fukuda, R.; Hasegawa, J.; Ishida, M.; Nakajima, T.; Honda, Y.; Kitao, O.; Nakai, H.; Vreven, T.; Throssell, K.; Montgomery Jr., J.A.; Peralta, J.E.; Ogliaro, F.; Bearpark, M.J.; Heyd, J.J.; Brothers, E.N.; Kudin, K.N.; Staroverov, V.N.; Keith, T.A.; Kobayashi, R.; Normand, J.; Raghavachari, K.; Rendell, A.P.; Burant, J.C.; Iyengar, S. S.; Tomasi, J.; Cossi, M.; Millam, J.M.; Klene, M.; Adamo, C.; Cammi, R.; Ochterski, J. W.; Martin, R.L.; Morokuma, K.; Farkas, O.; Foresman, J.B.; Fox, D.J. Gaussian 16 Rev. C.01, Wallingford, CT, 2016.

Gan, Z., Hu, X., Xu, X., Zhang, W., Zou, X., Shi, J., Zheng, K., Arslan, M., 2021. A portable test strip based on fluorescent europium-based metal–organic framework for rapid and visual detection of tetracycline in food samples. Food Chem. 354, 129501.

Guy Laurent Zanli, B.L., Tang, W., Chen, J., 2022. N-doped and activated porous biochar derived from cocoa shell for removing norfloxacin from aqueous solution: Performance assessment and mechanism insight. Environ. Res. 214, 113951.

Han, F., Huang, X., Mahunu, G.K., 2017. Exploratory review on safety of edible raw fish per the hazard factors and their detection methods. Trends Food Sci. Technol. 59, 37–48.

Hirsch, R., Ternes, T., Haberer, K., Kratz, K.-L., 1999. Occurrence of antibiotics in the aquatic environment. Sci. Total Environ. 225 (1), 109–118.

Hou, Z., Wang, X., Ikeda, T., Terakura, K., Oshima, M., Kakimoto, M.-a, Miyata, S., 2012. Interplay between nitrogen dopants and native point defects in graphene. Phys. Rev. B 85 (16), 165439.

Humphrey, W., Dalke, A., Schulten, K.J.J. o m g, 1996. VMD: Vis. Mol. Dyn. 14 (1), 33–38.

Jiang, D., Li, H., Cheng, X., Ling, Q., Chen, H., Barati, B., Yao, Q., Abomohra, A., Hu, X., Bartocci, P., Wang, S., 2023. A mechanism study of methylene blue adsorption on seaweed biomass derived carbon: From macroscopic to microscopic scale. Process Saf. Environ. Prot. 172, 1132–1143.

Jiang, L., Wei, D., Zeng, K., Shao, J., Zhu, F., Du, D., 2018. An Enhanced Direct Competitive Immunoassay for the Detection of Kanamycin and Tobramycin in Milk Using Multienzyme-Particle Amplification. Food Anal. Methods 11 (8), 2066–2075.

Jiang, W., Cai, Y., Liu, D., Yu, X., Wang, Q., 2024. Enhanced adsorption performance of oxytetracycline in aqueous solutions by Mg-Fe modified suaeda-based magnetic biochar. Environ. Res. 241, 117662.

Jing, Z., Ding, J., Zhang, T., Yang, D., Qiu, F., Chen, Q., Xu, J., 2019. Flexible, versatility and superhydrophobic biomass carbon aerogels derived from corn bracts for efficient oil/water separation. Food Bioprod. Process. 115, 134–142.

Kama, R., Liu, Y., Aidara, M., Kpalari, D.F., Song, J., Diatta, S., Sulemana, H., Li, H., Li, Z., 2024. Plant-Soil Feedback Combined with Straw Incorporation Under Maize/Soybean Intercropping Increases Heavy Metals Migration in Soil-Plant System and Soil HMRG Abundance Under Livestock Wastewater Irrigation. J. Soil Sci. Plant Nutr. 24 (4), 7090–7104.

Kaur Sodhi, K., Singh, C.K., 2022. Recent development in the sustainable remediation of antibiotics: A review. Total Environ. Res. Themes 3-4, 100008.

Li, H., Geng, W., Hassan, M.M., Zuo, M., Wei, W., Wu, X., Ouyang, Q., Chen, Q., 2021. Rapid detection of chloramphenicol in food using SERS flexible sensor coupled artificial intelligent tools. Food Control 128, 108186.

Li, H., Murugesan, A., Shoaib, M., Sheng, W., Chen, Q., 2024a. Functionalized metal-organic frameworks with biomolecules for sensing and detection applications of food contaminants. Crit. Rev. Food Sci. Nutr. 1–33.

Li, J., Cai, X., Liu, Y., Gu, Y., Wang, H., Liu, S., Liu, S., Yin, Y., Liu, S., 2020. Design and synthesis of a biochar-supported nano manganese dioxide composite for antibiotics removal from aqueous solution. Front. Environ. Sci. 8, 62.

Li, X., Cheng, H., 2023. Mn-modified biochars for efficient adsorption and degradation of cephalexin: Insight into the enhanced redox reactivity. Water Res. 243, 120368.

Li, X., Qian, Y., Guo, T., Fu, L., 2024b. DFT study on adsorption properties of TM(Ni, Co) Nx -doped graphene for high-temperature sensing of SF6 decomposed gases. Mater. Today Chem. 35, 101904.

Liu, H., Li, P., Qiu, F., Zhang, T., Xu, J., 2020. Controllable preparation of FeOOH/CuO@WBC composite based on water bamboo cellulose applied for enhanced arsenic removal. Food Bioprod. Process. 123, 177–187.

Liu, H., Shan, J., Chen, Z., Lichtfouse, E., 2021. Efficient recovery of phosphate from simulated urine by Mg/Fe bimetallic oxide modified biochar as a potential resource. Sci. Total Environ. 784, 147546.

Liu, J., Deng, Y., Li, X., Wang, L., 2016. Promising Nitrogen-Rich Porous Carbons Derived from One-Step Calcium Chloride Activation of Biomass-Based Waste for High Performance Supercapacitors. ACS Sustain. Chem. Eng. 4 (1), 177–187.

Liu, X., Shao, Z., Wang, Y., Liu, Y., Wang, S., Gao, F., Dai, Y., 2023. New use for Lentinus edodes bran biochar for tetracycline removal. Environ. Res. 216, 114651.

Lu, T., 2024. A comprehensive electron wavefunction analysis toolbox for chemists, Multiwfn. J. Chem. Phys. 161 (8).

Luo, J., Li, X., Ge, C., Müller, K., Yu, H., Huang, P., Li, J., Tsang, D.C.W., Bolan, N.S., Rinklebe, J., Wang, H., 2018. Sorption of norfloxacin, sulfamerazine and oxytetracycline by KOH-modified biochar under single and ternary systems. Bioresour. Technol. 263, 385–392.

Marimuthu, M., Arumugam, S.S., Sabarinathan, D., Li, H., Chen, Q., 2021. Metal organic framework based fluorescence sensor for detection of antibiotics. Trends Food Sci. Technol. 116, 1002–1028.

Picó, Y., Andreu, V., 2007. Fluoroquinolones in soil—risks and challenges. Anal. Bioanal. Chem. 387 (4), 1287–1299.

Qin, Y., Han, X., Yaruo, Z., Mingjiao, T., Chi, H., 2023. Research progresses of noble metal(Pt, Pd, and Ru) -based catalysts for catalytic decomposition of chlorine-containing volatile organic compounds. Energy Environ. Prot. 37 (03), 75–87.

Qiu, L., Li, C., Zhang, S., Wang, S., Li, B., Cui, Z., Tang, Y., Hu, X., 2023. Distinct property of biochar from pyrolysis of poplar wood, bark, and leaves of the same origin. Ind. Crops Prod. 202, 117001.

Quaik, S., Embrandiri, A., Ravindran, B., Hossain, K., Al-Dhabi, N.A., Arasu, M.V., Ignacimuthu, S., Ismail, N., 2020. Veterinary antibiotics in animal manure and manure laden soil: Scenario and challenges in Asian countries. J. King Saud. Univ. - Sci. 32 (2), 1300–1305.

Shakya, Amita, Vithanage, Meththika, Agarwal, T., 2022. Influence of pyrolysis temperature on biochar properties and Cr (VI) adsorption from water with groundnut shell biochars: Mechanistic approach. Environ. Res. 215, 114243.

Shoaib, M., Li, H., Khan, I.M., Hassan, M.M., Zareef, M., Niazi, S., Chen, Q., 2024. Emerging MXenes-based aptasensors: A paradigm shift in food safety detection. Trends Food Sci. Technol. 151, 104635.

Song, J., Lu, L., Wang, J., Li, X., Li, J., Wang, Q., Du, H., Xin, S., Xu, L., Yan, Q., Zhou, C., Liu, G., Xin, Y., 2023. Highly efficient nanocomposite of Y2O3@biochar for oxytetracycline removal from solution: Adsorption characteristics and mechanisms. Bioresour. Technol. 385, 129380.

Tian, Y., Chen, N., Yang, X., Li, C., He, W., Ren, N., Liu, G., Yang, W., 2023. Migration electric-field assisted electrocoagulation with sponge biochar capacitive electrode for advanced wastewater phosphorus removal. Water Res. 231, 119645.

UNEP Frontiers 2017: Emerging Issues of Environmental Concern; Nairobi: United Nations Environment Programme, 2017.

Verma, T., Aggarwal, A., Singh, S., Sharma, S., Sarma, S.J., 2022. Current challenges and advancements towards discovery and resistance of antibiotics. J. Mol. Struct. 1248, 131380.

Wang, H., Lou, X., Hu, Q., Sun, T., 2021. Adsorption of antibiotics from water by using Chinese herbal medicine residues derived biochar: Preparation and properties studies. J. Mol. Liq. 325, 114967.

Wang, L., Kuang, J., Chen, J., Mubula, Y., Gu, H., 2024. Adsorption differences of xanthate, dithiophosphate and dithiocarbamate on stibnite (010) surface with Cu2+ activated: Combined DFT calculations and experiments. Surf. Interfaces 51, 104483.
Wang, S., Jiang, X.M., Han, X.X., Wang, H., 2008. Fusion Characteristic Study on Seaweed Biomass Ash. Energy Fuels 22 (4), 2229–2235.
Wang, S., Wang, Q., Jiang, X., Han, X., Ji, H., 2013. Compositional analysis of bio-oil derived from pyrolysis of seaweed. Energy Convers. Manag. 68, 273–280.
Wei, M., Marrakchi, F., Yuan, C., Cheng, X., Jiang, D., Zafar, F.F., Fu, Y., Wang, S., 2022. Adsorption modeling, thermodynamics, and DFT simulation of tetracycline onto mesoporous and high-surface-area NaOH-activated macroalgae carbon. J. Hazard. Mater. 425, 127887.
Wu, J., Sun, X., Wu, J., Yu, X., 2025. Eggshell-enhanced biochar with in-situ formed CaO/Ca(OH)2 for efficient removal of Pb2+ and Cd2+ from wastewater: Performance and mechanistic insights. Sep. Purif. Technol. 354, 129352.
Wu, S., Liu, L., Duan, N., Li, Q., Zhou, Y., Wang, Z., 2018. Aptamer-Based Lateral Flow Test Strip for Rapid Detection of Zearalenone in Corn Samples. J. Agric. Food Chem. 66 (8), 1949–1954.
Xiansheng, Z., Jingwen, S., Zhifeng, L., 2023. Degradation of tetracycline hydrochloride by CoFe2O4/MnO2 activated permonosulfate. Energy Environ. Prot. 37 (05), 57–70.
Xue, J., Lei, D., Zhao, X., Hu, Y., Yao, S., Lin, K., Wang, Z., Cui, C., 2022. Antibiotic residue and toxicity assessment of wastewater during the pharmaceutical production processes. Chemosphere 291, 132837.
Xue, W., Shi, X., Guo, J., Wen, S., Lin, W., He, Q., Gao, Y., Wang, R., Xu, Y., 2024. Affecting factors and mechanism of removing antibiotics and antibiotic resistance genes by nano zero-valent iron (nZVI) and modified nZVI: A critical review. Water Res. 253, 121309.
Yang, L., Guo, X., Liang, S., Yang, F., Wen, M., Yuan, S., Xiao, K., Yu, W., Hu, J., Hou, H., Yang, J., 2023. A sustainable strategy for recovery of phosphorus as vivianite from sewage sludge via alkali-activated pyrolysis, water leaching and crystallization. Water Res. 233, 119769.
Yang, W., Cao, L., Lu, H., Huang, Y., Yang, W., Cai, Y., Li, S., Li, S., Zhao, J., Xu, W., 2024. Custom-printed microfluidic chips using simultaneous ratiometric fluorescence with "Green" carbon dots for detection of multiple antibiotic residues in pork and water samples. J. Food Sci. 89 (9), 5980–5992.
Zeng, K., Zhang, X., Wei, D., Huang, Z., Cheng, S., Chen, J., 2020. Chemiluminescence imaging immunoassay for multiple aminoglycoside antibiotics in cow milk. Int. J. Food Sci. Technol. 55 (1), 119–126.
Zhang, H., Song, X., Zhang, J., Liu, Y., Zhao, H., Hu, J., Zhao, J., 2022b. Performance and mechanism of sycamore flock based biochar in removing oxytetracycline hydrochloride. Bioresour. Technol. 350, 126884.
Zhang, J.B., Dai, C., Wang, Z., You, X., Duan, Y., Lai, X., Fu, R., Zhang, Y., Maimaitijiang, M., Leong, K.H., Tu, Y., Li, Z., 2023. Resource utilization of rice straw to prepare biochar as peroxymonosulfate activator for naphthalene removal: Performances, mechanisms, environmental impact and applicability in groundwater. Water Res. 244, 120555.
Zhang, S., Li, S., Li, D., Wu, J., Jiao, T., Wei, J., Chen, X., Chen, Q., Chen, Q., 2024. Sulfadiazine detection in aquatic products using upconversion nanosensor based on photo-induced electron transfer with imidazole ligands and copper ions. Food Chem. 456, 139992.
Zhang, T., Yuan, D., Guo, Q., Qiu, F., Yang, D., Ou, Z., 2019a. Preparation of a renewable biomass carbon aerogel reinforced with sisal for oil spillage clean-up: Inspired by green leaves to green Tofu. Food Bioprod. Process. 114, 154–162.
Zhang, T., Zhao, B., Chen, Q., Peng, X., Yang, D., Qiu, F.J.A.B.C., 2019b. Layer. Double hydroxide Funct. Biomass-.-. Carbon Fiber highly Effic. Recycl. Fluoride Adsorpt. 62, 1–7.
Zhang, Y., Chen, B., Zhang, L., Huang, J., Chen, F., Yang, Z., Yao, J., Zhang, Z., 2011. Controlled assembly of Fe3O4 magnetic nanoparticles on graphene oxide. Nanoscale 3 (4), 1446–1450.
Zhang, Z., Li, Y., Zong, Y., Yu, J., Ding, H., Kong, Y., Ma, J., Ding, L., 2022a. Efficient removal of cadmium by salts modified-biochar: Performance assessment, theoretical calculation, and quantitative mechanism analysis. Bioresour. Technol. 361, 127717.
Zhiyu, Y., Ke, Z., Zhenhao, X., Xiaodie, Z., Kai, Y., 2023. Research advance on the degradation of antibiotics through advanced oxidation technology using persulfate. Energy Environ. Prot. 37 (05), 1–14.
Zhou, H., Jiao, G., Li, X., Gao, C., Zhang, Y., Hashan, D., Liu, J., She, D., 2023. High capacity adsorption of oxytetracycline by lignin-based carbon with mesoporous structure: Adsorption behavior and mechanism. Int. J. Biol. Macromol. 234, 123689.
Zhou, X., Pan, W., Li, N., Salah, M., Guan, S., Li, X., Wang, Y., 2024. Development of a Sensitive Monoclonal Antibody-Based Colloidal Gold Immunochromatographic Strip for Lomefloxacin Detection in Meat Products. Foods (Basel, Switz.) 13 (16).